Zhengjun Liu

Aluminum oxide hard mask fabrication by focused ion beam implantation and wet etching

School of Electrical Engineering

Thesis submitted for examination for the degree of Master of Science in Technology.

Espoo 20.9.2012

Thesis supervisor:

Prof. Ilkka Tittonen

Thesis instructor:

D.Sc. (Tech.) Nikolai Chekurov

Aalto University
School of Electrical
Engineering

AALTO UNIVERSITY
SCHOOL OF ELECTRICAL ENGINEERING

ABSTRACT OF THE
MASTER'S THESIS

Author: Zhengjun Liu

Title: Aluminum oxide hard mask fabrication by focused ion beam implantation and wet etching

Date: 20.9.2012 Language: English Number of pages:7+70

Department of Micro- and Nanosciences

Professorship: Physics of micro technologies Code: S-129

Supervisor: Prof. Ilkka Tittonen

Instructor: D.Sc. (Tech.) Nikolai Chekurov

A novel aluminum oxide (Al_2O_3) hard mask fabrication process with nanoscale resolution is introduced in this work. The Al_2O_3 mask can be used for various purposes, and in this thesis it was utilized for silicon patterning using cryogenic deep reactive ion etching (DRIE). Patterning of Al_2O_3 is a two-step process utilizing focused ion beam (FIB) irradiation combined with wet etching. Ga^+ FIB maskless patterning renders wet etch selectivity between the irradiated region and the non-irradiated region on the Al_2O_3 layer, and mask patterns can be easily revealed by wet etching. This method is a modification of direct Ga^+ FIB implantation for silicon etch stop. Introducing an Al_2O_3 layer eliminates the lattice damage and doping to silicon substrate in critical devices, as an extra film protects the underlying silicon from Ga^+ ions. Masking capacity is evaluated in terms of equal width line and space pairs amount per 1 μm in a nano-line array. 7 pairs per 1 μm is achieved in this work.

Keywords: FIB, photoresist-free, aluminum oxide, hard mask, cryogenic DRIE, nanofabrication

Preface

First of all, I would like to acknowledge Professor Ilkka Tittonen for providing me the opportunity to work in this interesting field. Moreover, I sincerely appreciate his supervision, guidance and help through this work.

I am truly grateful to Nikolai Chekurov, for all his explicit instruction, patient guidance, smart advices and always prompt help. His persistent accomplishment has also been encouraging me to improve myself in career.

Thanks are due to co-worker Kari Iltanen as well, for his positive collaboration and contribution to this work.

I also wish to thank Ken Pennington for lauguage assistance.

I would like to take this opportunity to extend my appreciation to Victor Ovchinnikov, Kestas Grigoras, Antti Niskanen and Ville Vähänissi, who have helped me to make a good start of my studies in a new field.

My deep gratitude goes to my parents and Otto, for their support, encouragement, understanding and sharing my thoughts through the duration of my studies. Finally, I wish to thank all my friends for support and times of joy and fun.

Otaniemi, 20.9.2012 Zhengjun Liu

Contents

Abstract ii

Preface iii

Contents iv

Symbols and abbreviations vi

1 Introduction 1

2 Theory and background 3

2.1 Lithography . . . 3

2.1.1 Optical lithography . . . 3

2.1.2 Electron beam lithography . . . 6

2.1.3 Proximity X-ray lithography . . . 7

2.1.4 Nanoimprint lithography . . . 7

2.2 Etching . . . 8

2.2.1 Etching profiles . . . 9

2.2.2 Wet etching . . . 11

2.2.3 Plasma etching . . . 12

2.2.4 Etch mask and effect on etch process . . . 15

2.3 Al_2O_3 as an etch mask for silicon . . . 16

2.4 Atomic layer deposition (ALD) . . . 18

2.4.1 The principle of ALD . . . 18

2.4.2 Al_2O_3 growth by ALD . . . 19

2.4.3 Compound and single element ALD materials . . . 20

2.4.4 ALD applications in microelectronics . . . 20

2.4.4.1 Electroluminescent display phosphors . . . 20

2.4.4.2 High permittivity (high-$\varkappa$) dielectrics . . . 21

2.4.4.3 Transparent conductors . . . 21

2.4.4.4 Passivation and diffusion barriers . . . 22

2.5 Ion implantation . . . 23

2.5.1 Ion-surface interaction . . . 23

2.5.2 Ion implantation simulation 26
2.5.3 Ion implantation applications 29
2.6 Focused ion beam (FIB) technology 29
2.6.1 FIB system introduction 29
2.6.2 Principles of FIB imaging, milling, deposition and implantation . 32
2.6.3 FIB applications in micro- and nanofabrication 35
2.6.3.1 FIB milling 35
2.6.3.2 FIB deposition 37
2.6.3.3 Surface modification with FIB system 38

3 Experimental section 42
3.1 Simulation of ion distribution 42
3.2 Hard mask fabrication and silicon etching 42
3.2.1 Mask fabrication and silicon DRIE process overview 42
3.2.2 Al_2O_3 mask preparation 44
3.2.3 Inductively coupled plasma etching 46

4 Results and discussion 47
4.1 Optimization of masking layer parameters 47
4.1.1 Testing dose selection 47
4.1.2 Wet etching of FIB patterned mask 52
4.2 Al_2O_3 mask characterization 55
4.2.1 Selectivity 55
4.2.2 Resolution 55

5 Conclusions and outlook 62

References 64

Symbols and abbreviations

Symbols

d	thickness
E	energy
E_b	binding energy
E_d	displacement energy
E_f	final energy
ϕ	ion dose
k_1, k_2	coefficients of process-related factors in projection systems
k_e	stopping power proportionality constant
κ	permittivity
λ	wavelength
M	ion mass
NA	numerical aperture
n	Gaussian depth-concentration profile
p	impact parameter
r	atomic radius
R	resolution (in Section 2.1.1)
R	mean range (in Section 2.5.2)
R_p	mean projected range
ΔR_p	straggle
S_n	nuclear stopping component
S_e	electronic stopping component
S_p	proton stopping power
S_{Z_1}	desired stopping power of the partially stripped ion
v	velocity
v_0	Bohr velocity = 2.2×10^8 cm/s
x	length of travel
Z_1	ion atomic number
Z_1^*	stopping power effective charge

Abbreviations

AFM	atomic force microscope
ALD	atomic layer deposition
ALE	atomic layer epitaxy
BCA	binary collision approximation
CCP	capacitively coupled plasma
CMOS	complementary metal oxide semiconductor
DOF	depth of focus
DRAM	dynamic random access memory
DRIE	deep reactive ion etching
EOT	equivalent oxide thickness
FIB	focused ion beam
FWHM	full width at half-maximum
IC	integrated circuit
ICP	inductively coupled plasma
ITO	indium tin oxide
LED	light emitting diode
LMIS	liquid metal ion source
MEMS	microelectromechanical systems
MOSFET	metal oxide semiconductor field effect transistor
PECVD	plasma enhanced chemical vapor deposition
RF	radio frequency
RIE	reactive ion etching
SE	secondary electron
SEM	scanning electron microscope
SI	secondary ion
SIMS	secondary ion mass spectroscopy
SOI	silicon on insulator
SRIM	stopping and range of ions in matter
SRR	split-ring resonator
TCO	transparent conducting oxide
TFEL	thin film electroluminescent
TMA	trimethyl aluminum
TMAH	tetramethylammonium hydroxide
TRIM	transport of ions in matter
UV	ultraviolet

1 Introduction

Pattern transfer onto silicon wafers or other substrates is a fundamental requirement for device manufacturing in micro- and nanofabrication. The transfer of micro- and nanopattern typically involves two steps: lithography for masking resist and mask pattern replication to underlying substrate or thin film by etching. Each process mentioned above directly determines the quality of the final device.

Lithography is crucial for pattern element definition in semiconductor industry. As the conventional method, optical lithography (photolithography) has been the most widely used technology, due to sufficient accuracy and throughput, especially for mass production. As 1 μm resolution is considered a formidable barrier for photolithography taking into account the cost issue, new techniques have been developed for nanostructure fabrication.

Maskless direct patterning techniques, such as electron beam lithography, ion beam lithography and X-ray lithography, provide reliable higher resolutions than photolithography at the expense of throughput. An alternative approach for pattern transfer using mechanical press has been provided by nanoimprint lithography. It is a cost effective method with high resolution and throughput. However, the alignment complications raise overlay accuracy problems.

Mask quality is also an aspect which affects pattern transfer quality. Properties, such as sidewall conformation, adhesion to the substrate and selectivity against the target material, confine the accuracy of critical dimension and the sidewall condition of the structure, especially for deep etching. Soft masks, most often in the form of photoresist, fulfill the etching requirement in many cases. Under tough etch conditions, such as anisotropic wet etching of silicon or deep reactive ion etching (DRIE), soft mask may fail and hard mask is required. Silicon dioxide, silicon nitride and aluminum oxide are common hard mask materials.

Reliable and high resolution masks for silicon etching is demanded for microfabrication. Aluminum oxide (Al_2O_3) is noticed for its extremely high selectivity against silicon in deep reactive etching processes. It is competent for hundreds micrometers or through wafer etching and high aspect ratio silicon structure etching with controllable sidewall condition. Al_2O_3 mask patterning by optical lithography gives the resolution at micrometer level. The resolution can be further improved by alternative patterning methods such as electron beam lithography.

Focused ion beam (FIB) process provides multiple functions in micro- and nanofabrication. It involves surface bombardment of the specimen by ions which can be used for ion implantation, imaging, substrate milling and material deposition. It is also a maskless direct writing process providing precise digital patterning pixel by pixel. Direct FIB milling is commonly used for selective material etching. Surface modification by FIB can also render etching selectivity of ion treated region to the non-treated one for certain materials which can be applied for foreign mask free etch stop. A well known example is that high concentration p^+-doped silicon has dramatically reduced etch rate in alkaline etchants.

This work introduces a novel method for Al_2O_3 mask patterning for silicon deep reactive ion etching (DRIE) utilizing FIB patterning combined with wet etching. This process is a modification of a foreign mask free gallium FIB patterning process for silicon etching, which eliminates the lattice damage and doping to silicon substrate in critical devices. Gallium ion irradiation increases the wet etch rate of Al_2O_3 in both acid and alkaline etchants. Shallow surface gallium FIB irradiated Al_2O_3 mask protects the underlying silicon from gallium ions. Mask pattern can also be easily formed by wet etching. Masking capacity is evaluated as equal width line and space pairs amount per 1 µm, which is 7 pairs per 1 µm for best achieved result in this work.

2 Theory and background

2.1 Lithography

Lithography in microfabrication refers to the process of defining shapes on the surface of a semiconductor wafer. Typically it involves the selective removal of a photosensitive soft mask already deposited on the wafer. Currently the patterning techniques can be divided into two main categories, pattern replication and maskless direct writing by pattern generator. In pattern replication, a master pattern image is used for parallel pattern transfer. The most widely used replication approach is to pattern a photosensitive soft mask with projectional energetic particles through a photomask, known as optical lithography. Alternatively, a reticle mould with three dimensional patterns on the surface can be used for soft mask patterning by mechanical deformation. A representative technique for mould replication is nanoimprint. On the other hand, pattern generator accepts digital pattern input data and directly writes the physical image on a substrate or a thin film layer, using either charged particles or photons. The main disadvantage of direct writing lithography is the low imaging throughput no more than one 200 mm wafer per hour, while the general rule for economical mass production requires a throughput in the order of 60-100 wafers per hour.[1] Electron beam and ion beam are the most commonly used energetic particle sources for maskless lithography.

2.1.1 Optical lithography

Optical lithography has been the dominating patterning method in semiconductor manufacturing despite that the replacing techniques have often been predicted. Standard optical lithography process starts with photosensitive resist (photoresist) deposition on a wafer, typically by spin coating followed by baking to remove the solvent. After the alignment of the photomask and the wafer, photoresist is exposed by ultraviolet (UV) radiation. Exposure changes the solubility which enables selective removal of resist according to mask pattern in the developer. In the case of positive photoresist, the exposed area dissolves during the development. In contrast, the UV exposed area of a negative photoresist becomes insoluble in the developer.

The simplest lithographic technique is contact lithography, in which the photomask is placed directly on top of a resist covered wafer with intimate contact. Figure 1 illustrates the schematic process of contact lithography utilizing negative photoresist on a silicon substrate. Theoretically the image ratio between mask dimension and final dimension is 1:1, while the resolution is also affected by diffraction at mask edges. The resolution is limited by the mask cost since the submicron featured mask is excessively costly.[2] Damage subjected to the mask is frequent due to the contact mode and the mask repair is a time consuming process. As a result, contact printing is not an effective method for production.

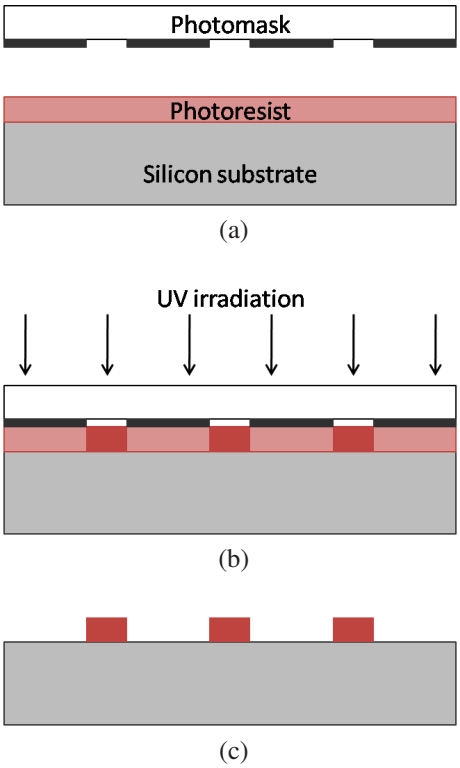

Figure 1: Schematic drawing of contact lithography process with negative photoresist: (a) photomask aligning to a photoresist coated substrate; (b) substrate approaching to photomask and photoresist exposure to light irradiation; (c) patterned photoresist on the silicon substrate after development.

Proximity lithography is a modification of contact lithography, in which a small gap is left between the mask and the wafer as shown in Figure 2. In proximity printing, wavefront diffraction at the gap and the uneven flatness across the wafer lower the resolution and generate overlay problems. Thus the resolution is typically worse than 5 μm.[3]

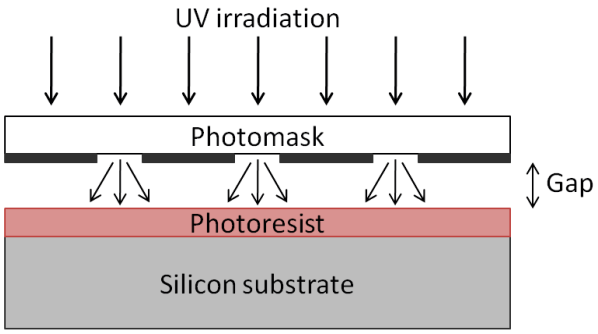

Figure 2: Schematic illustration of proximity lithography.

Projection lithography is a method that improves the resolution and resolves overlay problems of proximity lithography while keeping no contact with the wafer. As illustrated

in Figure 3, in projection lithography machines, optical lens system is placed in the gap between the photomask and the wafer. UV light transmitted through the photomask is collected by the lens system, which projects the image onto the photoresist coated wafer, typically with a 1:1 (1×) or reduction magnification. The reduction magnification allows making photomask features with magnified dimensions compared to the original values.

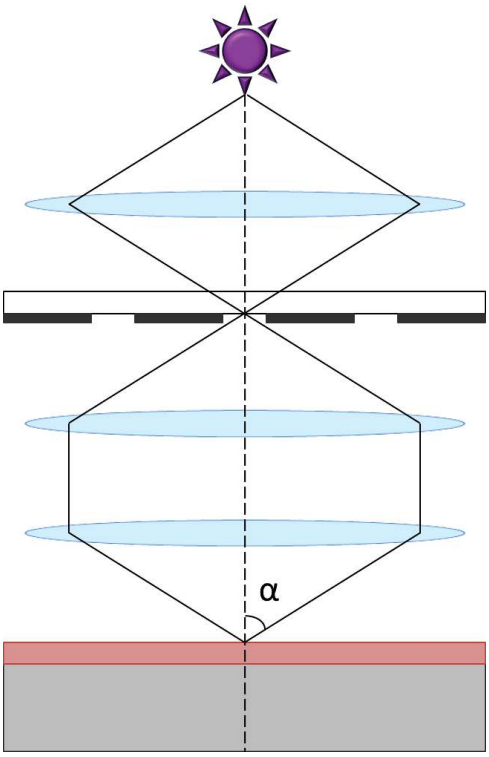

Figure 3: Schematic illustration of projection lithography.

Projection optics also provides the combination of serial and parallel writing method and allows chipwise exposure. The primary tool for chipwise exposure is the stepper with reticle as photomask. Steppers exist in two configurations, step-and-repeat or step-and-scan. In a step-and-repeat system, only a chip field is exposed at one time and the wafer is moved to a precise position so that another chip can be exposed. In a step-and-scan system, only part of the reticle and therefore also part of the wafer will be illuminated, and the entire wafer is exposed by scanning the reticle and wafer synchronously. Steppers are the most commonly used lithographic tools in advanced integrated circuit (IC) fabrication. Reticle to wafer ratio can reach 10:1 taking advantage of reduction optics. Thus theoretically 1 μm mask feature size will give a resolution down to 100 nm order. The advantages of a stepper with high precision come at a price of tens of million dollars. Besides, the throughput of chipwise exposure with steppers is lower than that of full wafer projection exposure. For example, at the introduction of step-and-repeat systems, the throughput was approximately 25 wafers per hour, while that of 1× projection optical systems was 100 wafers per hour.[4]

The resolution in conventional projection optical lithography is approximated by Rayleigh

relations. The resolution R and the corresponding depth of focus (DOF) are given by the following equations:

$$R = k_1 \lambda / NA \tag{1}$$

$$DOF = k_2 \lambda / NA^2 \tag{2}$$

where λ is the exposure wavelength, NA is the numerical aperture of the optical system, and k_1 and k_2 are constants depending on the specific resist material, process technology and imaging accuracy which have been aggressively scaled down recently.

According to Equation 1 and Equation 2, to reduce the wavelength and to improve the lens system capabilities are the fundamental methods to obtain higher resolutions. Usually the best achievable resolution with mercury arc UV light lithography is in the range of 0.5-1 μm,[4] which leads to the development of short wavelength light exposure techniques such as deep UV lithography, deep UV immersion lithography and extreme UV lithography. For example, critical dimension of 180 nm is achieved in mass production by using KrF excimer laser with a wavelength of 248 nm, in combination with resolution enhancement techniques such as off-axis illumination, phase-shift mask, optical proximity correction, as well as applying advanced resist materials.[5] Wavelength can be further reduced using ArF and F_2 excimer lasers which give wavelengths of 193 nm and 157 nm respectively. Commercial photolithography systems using deep UV light at the wavelength of 193 nm with water immersion lenses are available which can be used to produce microelectronics containing features with a half-pitch as small as 40 nm.[6] Extreme UV lithography has been under development which extends optical lithography to a higher resolution theoretically by utilizing a shorter imaging wavelength 13.5 nm. However, wavelength reduction to extreme UV level raises new challenges including high power light source development, suitable photoresist material exploration and imaging system adaption.

2.1.2 Electron beam lithography

The use of electron beam instead of photons as the exposure source in lithography combined with a high DOF has led to extremely high resolution. Linewidth under 10 nm can be patterned reproducibly.[3] The digital control of electron beam position enables accurate maskless patterning for electron sensitive photoresist at the cost of throughput. Electron beam lithography is mainly used for photomask production, nanostructure prototyping, device verification studies and small scale production of specific devices. The throughput of electron beam lithography can be enhanced in a sense by modifying the beam size according to the pattern and parallel exposure for repetitive structures. Electron projection lithography with the aid of optical lenses and apertures similar to UV lithography is a more promising method for throughput improvement.

2.1.3 Proximity X-ray lithography

X-ray lithography uses exposure source with short wavelength around 1 nm and proximity techniques for photoresist patterning. Due to the wavelength of X-rays, resolution is less problematic with proximity print. Since no focusing optics in the conventional sense are required, the equivalent DOF is generally quite large. X-ray lithography is also applicable for stepped substrate.

Since X-ray absorption depends on the atomic number of the material and most materials have low transparency at x-ray wavelength range, the mask substrate must be thin membrane (under 5 μm thick, typically 1-2 μm) made of low atomic number material, such as silicon carbide, silicon, silicon nitride or diamond. The pattern is on the other hand defined by a relatively high atomic number material (approximately 0.5 μm thick), such as tantalum, tungsten, gold or one of their alloys. Due to the similar thicknesses of the thin mask membrane and the absorber layer on it, mask fabrication is generally considered the most challenging part of this technique.[7]

2.1.4 Nanoimprint lithography

Nanoimprint lithography is a simple and high throughput replication technique. As shown in Figure 4, it creates patterns by physical pressing of the master against a deformable resist coated substrate. After the mechanical deformation of the resist the master is released and the resist residue at the substrate bottom is removed by plasma etching. By this means the resolution is not limited by the light source wavelength and optical projection techniques as in photolithography. Besides nanoimprint also overcomes the low throughput in direct writing lithography. As a result nanoimprint is applicable for mass replication of nanostructures with features smaller than 10 nm.[8] A positive sidewall profile of nanoimprint patterned resist is demanded for easy master release, which limits the application of nanoimprint in lift-off process.

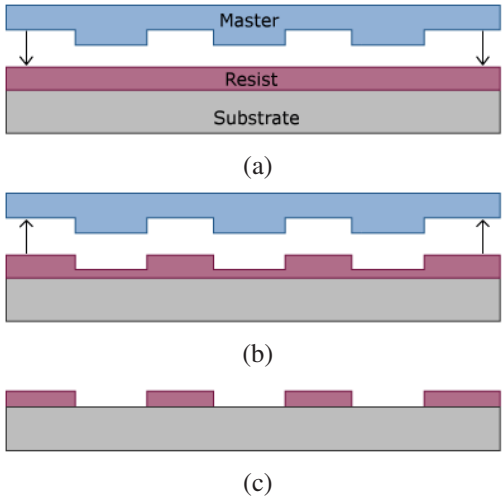

Figure 4: Schematic process flow of nanoimprint lithography: (a) master imprinting to create a thickness contrast in a resist; (b) master release; (c) resist residual removal in the compressed areas by RIE.[8]

2.2 Etching

Pattern transfer process contains two steps: lithographic masking layer patterning and the subsequent etching of the underlying material. Etching refers to a process by which material is removed from the wafer, either from the silicon substrate itself or other material layer on the wafer, which can be applied to both thin film and bulk material. Material is chemically and/or physically attacked and eroded in the unprotected areas during etching. Some materials can be etched spontaneously by chemical etchant, such as silicon by fluorine, aluminum by chlorine and silicon oxide by hydrofluoric acid. In some cases physical processes such as ion bombardment are needed to assist the etching process. Etching processes are often divided into two classes, wet etching and dry etching. Plasma etching is the most commonly used dry etching method. Dry etching processes that do not involve plasma also exist, for example hydrogen fluoride (HF) vapor release etching. Etch rates are typically 100-1000 nm/min for both wet and plasma processes. The lower limit comes from manufacturing economics and the upper limit is restricted by resist degradation, thermal runout and damage issues. Silicon etching has exceptional high rates up to 20 μm/min in both wet etching ($HF:HNO_3$) and plasma etching (DRIE in SF_6).[4] Etching techniques from both classes have been well established for silicon processing. Additionally, masking effects during silicon etching is also a well studied issue. Masks with high selectivity to the substrate, good adhesion to the surface, and patternable high resolution are especially demanded in the fabrication of high aspect ration structures with controlled sidewall condition. Other technologies for silicon processing are available such as laser drilling,[9] ultrasonic drilling,[10] ion beam milling and electron beam milling.

Figure 5 demonstrates a commonly used silicon etching process with silicon dioxide (SiO_2) hard mask. When hard mask is applied, patterns are firstly transferred onto the hard

mask by photolithography and hard mask layer etching. As shown in Figure 5, a SiO_2 layer is deposited on the silicon substrate (Figure 5a) by for example plasma enhanced chemical vapor deposition (PECVD), and a photoresist is applied on the SiO_2 layer by spin coating (5b). After the UV exposure of the photoresist through a photomask (Figure 5c), the photoresist is developed and cured which will serve as the etch mask of the SiO_2 layer (Figure 5d). Next, patterns are realized on the SiO_2 layer by reactive ion etching (Figure 5e) followed by photoresist removal (Figure 5f). Then the patterns are transferred to the substrate by silicon etching, for example DRIE (Figure 5g).

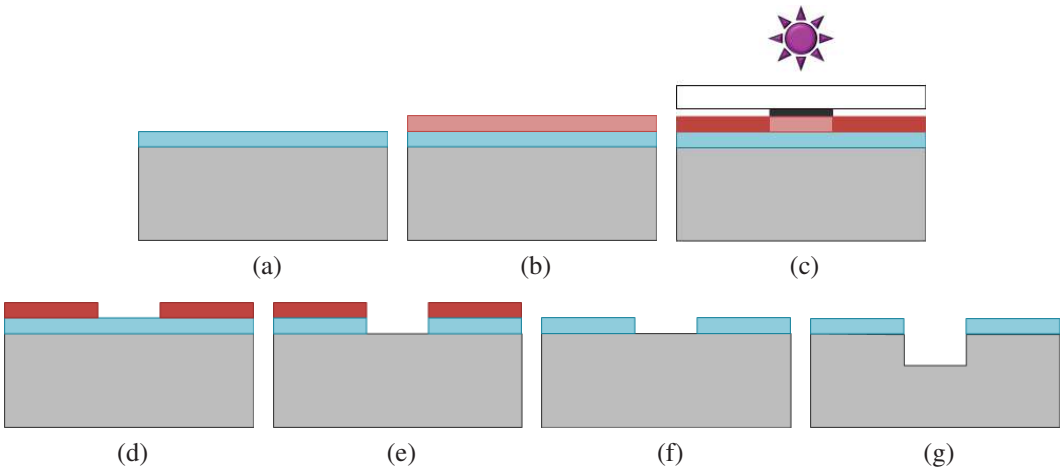

Figure 5: Schematic illustration of a typical lithography and etching process with SiO_2 hard mask: (a) SiO_2 deposition; (b) photoresist spin on and soft bake; (c) UV exposure of the photoresist through a photomask and post exposure bake; (d) photoresist development and cure; (e) SiO_2 mask etching; (f) photoresist removal; (g) silicon etching.

2.2.1 Etching profiles

Etching profiles fall into two categories, isotropic and anisotropic, which are compared in Figure 6. In isotropic etching, the etch front proceeds as a spherical wave from all directions exposed to the etchant. As a result, the etch front also proceeds under the mask and leads to undercut. For this reason it cannot be used to make fine features. On the other hand, undercut is sometimes desirable and even necessary in the fabrication of certain structures such as suspended beams and plates, cantilevers and fine tips.

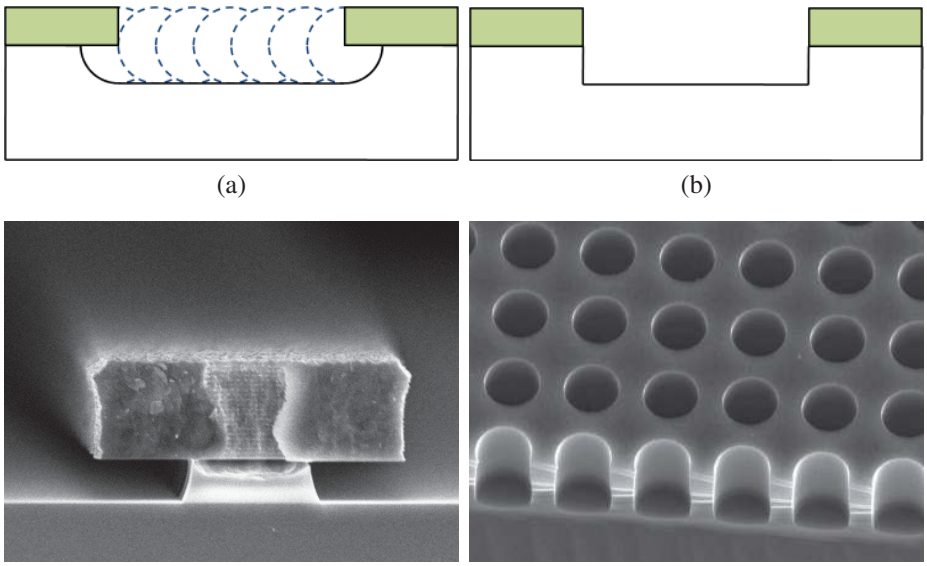

Figure 6: Schematic profiles of (a) isotropic and (b) anisotropic etching, and application examples of (c) isotropic and (d) anisotropic etching[11].

Anisotropic plasma etching is associated with vertical or almost vertical sidewall profile, which is suitable for patterning fine structures. In real practice of plasma etching, etching profiles are seldom vertical for high aspect ratio structures, especially when the loading is low. Sidewall profile can be tailored by optimizing process parameters such as pressure, power, temperature and gas flow. Sidewall passivation and cryogenic operation temperature can also help to decrease the sidewall slope.

Due to the crystal orientation-dependent etch rate of silicon in alkali etchant, anisotropic wet etching is also applicable for silicon. The schematic illustration of anisotropic wet etching profile of <100> silicon wafer is depicted in Figure 7. Etching profile is initially determined by the fast etching crystal planes (100) and (110), and terminates when slow etching (111) planes are revealed. The angle between the (111) and (100) planes is 54.7°, which is a characteristic feature for anisotropically wet etched silicon microelectromechanical systems (MEMS) structure.

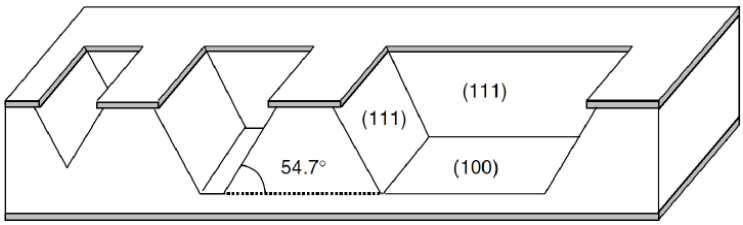

Figure 7: Anisotropic wet etching profiles in <100> silicon wafer. The sloped sidewalls are the slow etching (111) planes and the horizontal planes are fast etching (100) planes. Etching stops when slow etching (111) planes meet.[2]

2.2.2 Wet etching

Wet etching processes are theoretically simple and available for most materials, with diamond and GaN being the most notable exceptions.[4] Some etching solutions for common materials and the corresponding etch rates are shown in Table 1.[12] Chemical reactions are usually strongly temperature dependent. Uniform temperature control, especially for reactions with heat evolution, can be problematic which is not favorable for maintaining a stable etching process. Reaction products may affect the etching process in different ways, for example to catalyze or inhibit the reaction. Volatile products may also impede the reaction surface from being exposed to etchant solution.

Target material	Etchant	Etch rate
Poly-Si	HNO_3 (72%):HF (38%):CH_3COOH (98%) = 2:1:1	15 μm/min (25 ºC)
SiO_2	HF (48%):NH_4F (40%) = 1:15	100 nm/min (25 ºC)
Si_3N_4	H_3PO_4:H_2O = 9:1	10 nm/min (180 ºC)
Al	H_3PO_4O (85%):HNO_3 (65%):H_2O = 20:1:5	220 nm/min (40 ºC)

Table 1: Common wet etchants for listed materials and the corresponding etch rates.[12]

Wet etching of silicon can give both isotropic and anisotropic profiles, depending on the etchant. Wet etchant with the composition HF:HNO_3:CH_3COOH:H_2O is commonly used for silicon isotropic wet etching. Two processes are involved in the etching reaction. First HNO_3 oxidizes silicon to form silicon dioxide, and HF etches the silicon dioxide hereby formed. The addition of acetic acid improves wetting of the hydrophobic silicon surface; it also increases and homogenizes the etch rate. Isotropic etching is mainly applied when undercut is desirable. Some typical examples are free standing membranes, bridges and cantilevers releasing, sacrificial layer removal and reservoir formation. The main limitations of wet etching are due to the complications of surface chemical reaction.

Anisotropic wet etching of silicon is utilized for many key applications in microsystems technology. Silicon etch was found to be orientation-dependent and concentration-dependent in some chemical solutions in the 1960s.[13] Taking advantage of this property, many surface micromechanical and silicon on insulator (SOI) devices are achieved for auxiliary structures, even though the main device features are defined by plasma etching. Single crystal silicon exhibits different etch rates for individual crystal orientation in strong alkaline substances such as aqueous potassium hydroxide (KOH) and tetramethylammonium hydroxide (TMAH) solutions. Since the bonding energy of silicon atoms is characteristic for each crystal plane, all the alkaline etchants share the same basic features of etching (100) crystal planes faster than (111) crystal planes. KOH exhibits 200:1 selectivity between (100) and (111) planes, while the selectivity is 30:1 in TMAH.[4] Anisotropic silicon etching is a method to make through wafer opening.

It is also widely used for the fabrication of structures such as deep groove, V-shape groove and sharp tip. Figure 8 and Figure 9 give an illustrative presentation of silicon sharp tips fabricated on <100> and <111> silicon wafers, using anisotropic etching in surfactant modified TMAH solutions at 80 ºC. Tips with aspect ratio of 0.8:1 and average radius of curvature of 6 nm can be obtained on <100> wafer, and tips with higher aspect ratio reaching 6:1 and smaller average radius of curvature down to less than 2 nm can be obtained on <111> wafer.[14]

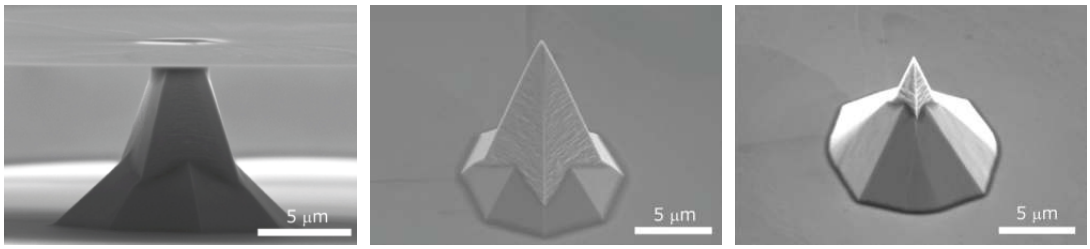

(a) (b) (c)

Figure 8: Etch process for sharp tip fabrication on <100> silicon wafer by anisotropic etching in 25wt% TMAH solutions at 80 ºC: (a) early etch stage with SiO_2 circular mask; (b) latter etch stage after mask drops; (c) completed tip after tip sharpening with surfactant addition.[14]

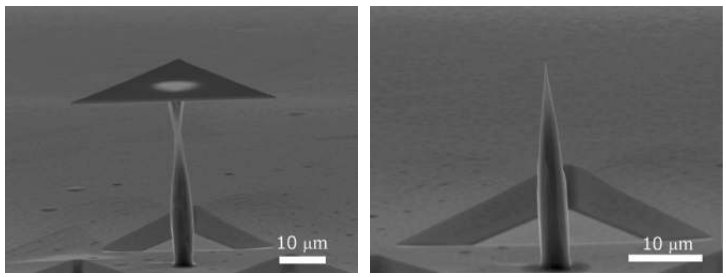

(a) (b)

Figure 9: Etch process for sharp tip fabrication on <111> silicon wafer by anisotropic etching in surfactant modified TMAH solutions at 80 ºC: (a) intermediary etch stage before mask cap drops; (b) completed tip.[14]

2.2.3 Plasma etching

Plasma etching is a key technology for pattern transfer to a wafer in semiconductor, MEMS and integrated circuit manufacturing. Reactive ion etching (RIE) is a specific type of plasma etching utilizing the combination of ion assisted physical etching and chemical etching. It possesses the advantage of good profile control to perform highly anisotropic etching which yields vertical or near vertical sidewalls. With anisotropy, RIE gives directional removal independent of the silicon crystal orientation. RIE is done in a vacuum chamber by reactive gases excited by radio frequency (RF) fields. During RIE, reactive radicals and ions are generated in plasma which reacts with a solid

surface, resulting in selective removal of material. The plasma density depends on the bombardment strength in RIE reactors, thus strong bombardment is required to produce highly anisotropic etching. Strong bombardment results in excessive etch mask erosion, which forces the use of thick photoresist or hard mask.

Plasma etching is based on volatile reaction products. Oxygen atoms can be effectively used as etchants for photoresist which forms oxycarbide. Fluorine, chlorine and bromine processes are standard silicon etch methods which result in volatile silicon halogenate reaction products at room temperature at millitorr pressures. Fluorine processes are seldom fully anisotropic, but are less toxic and safer to use compared to chlorine and bromine processes. Argon and SF_6 (Ar/SF_6) gas mixture is a common combination for silicon etching. Silicon nitride (Si_3N_4) can be etch by fluorine. SF_6^- and SF_4^- based processes for nitride etching provide no selectivity against silicon and approximately 2:1 selectivity against silicon dioxide. On the other hand, CHF_3^- based processes etch nitride and provide selectivity against silicon. After native oxide removal by ion bombardment, aluminum (Al) can be spontaneously etched by Cl_2.[4]

RIE can be modified to create very deep etching profiles with almost vertical sidewalls. While typical RIE rates are on the order of 0.1-1 μm/min, deep reactive ion etching (DRIE) rates can reach 2-20 μm/min without sacrificing the etch profile quality.[4] Two major variants of DRIE are Bosch and cryogenic processes, which take advantage of sidewall passivation mechanisms in different ways.

Bosch process proceeds by time-multiplexed gas pulse alternation. Each periodic loop of Bosch process for silicon etching consists of two subsequent steps: etching and passivation. As shown in Figure 10,[15] SF_6 plasma is firstly pulsed to etch a few microns of silicon with isotropic profile. Subsequently C_4F_8 pulse is applied for conformal coverage of protective fluoropolymer over the wafer surface. The next step is the second etch by SF_6 for the protective polymer removal from the trench bottom, meanwhile the sidewalls remain protected. After removing of protective film from the bottom the next periodic loop proceeds until the required etch depth is reached. A 3D simulated Bosch process etch profile of a 2 μm × 2 μm cross trench is shown in Figure 11, which clearly demonstrates the scalloped sidewall roughness.[16] Sidewall roughness can be reduced by optimizing the duration of the etch and passivation steps[17] or post etch processing. Some available post etch processes include thermal oxidation followed by oxide etching[18], annealing in a hydrogen atmosphere at high temperature[19] and low concentration alkaline solution etching at low temperature[20].

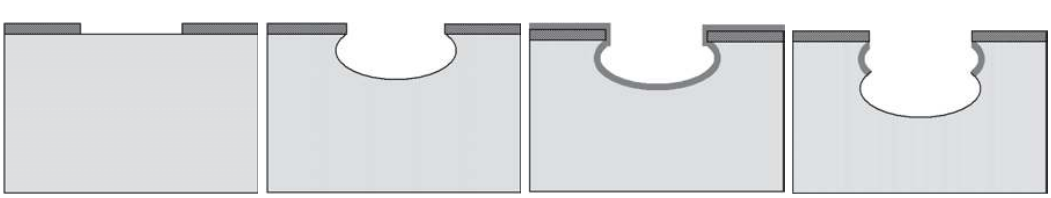

Figure 10: Time-multiplexed Bosch process: (a) mask patterning; (b) SF_6 isotropic etching; (c) C_4F_8 passivation film deposition; (d) next etch step.[15]

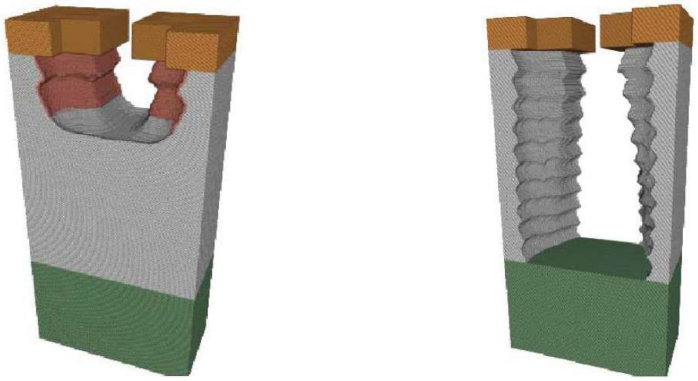

(a) (b)

Figure 11: Simulated Bosch process etch profile of a 2 μm × 2 μm cross trench: (a) interval process; (b) final result.[16]

In cryogenic DRIE, continuous SF_6/O_2 flow is used at cryogenic temperatures below -100 ºC. Etching and passivation processes take place simultaneously to form vertical etch profile. A protective SiO_xF_z film from the reaction products is deposited on the cooled feature walls and is removed from horizontal surfaces by ion bombardment, leaving the sidewalls protected. Lateral chemical etching is also suppressed by low temperature. Contrary to Bosch process, cryogenic DRIE leads to smooth sidewall profile.

Undercut is an unavoidable issue in silicon DRIE. The common explanation for it is the isotropic component in the etch process. In a recent study, it is revealed that deposition of passivation film can be the primary cause of undercut. Figure 12 shows the undercut evolution during Bosch process deep silicon etching. Undercut is not visible after 2 minutes etching. The scallop formed by the first cycle is smaller than those formed by subsequent cycles. This is due to the native oxide which impedes the first etch step and results in the formation of partial scallop. 150 nm undercut starts to be observed after 20 minutes, which is approximate to the scallop depth after 2 minutes. The scallops also start to become smooth. After 40 minutes undercut reaches 900 nm and the sidewall becomes smooth and sloped. The authors attribute this observation to the nonuniform deposition of passivation film on surface with different angular direction. Passive deposition preferentially takes place on the upside of each scallop leaving the underside of each scallop relatively unprotected. Preventing undercut requires a much more isotropic deposition step of passivation film.[21]

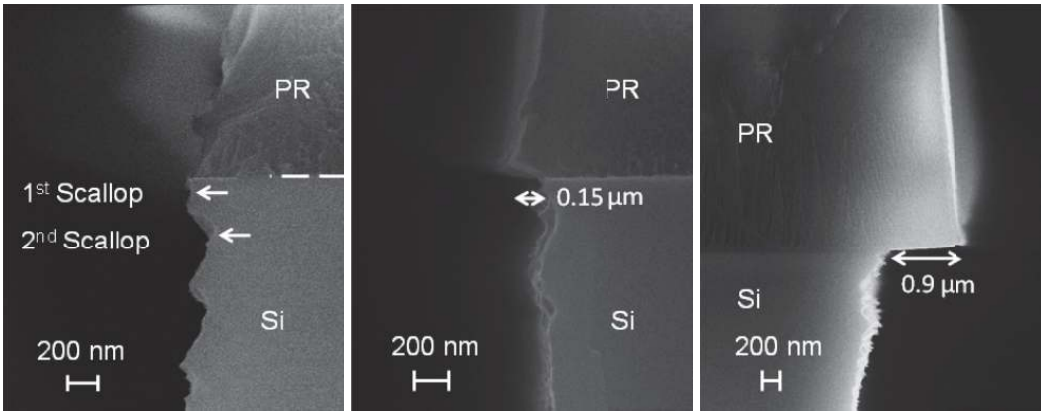

(a) (b) (c)

Figure 12: Scanning electron microscope (SEM) images of the development of mask undercut during Bosch process DRIE of silicon: (a) after 15 cycles (2 minutes), undercut is not visible; (b) after 150 cycles (20 minutes), undercut approximating to the lateral depth of the first scallop is observed; (c) after 300 cycles (40 minutes), undercut reaches 900 nm and the sidewall becomes smooth and sloped.[21]

2.2.4 Etch mask and effect on etch process

Mask properties, including sidewall conformation, adhesion to the substrate and selectivity, are significant issues in silicon etch process, which confine the smallest critical dimension of the finally achieved structure and affect the sidewall condition of silicon. When photoresist is applied as etch mask, usually a vertical sidewall is desirable and necessary for the best linewidth control in plasma etching. However due to light diffraction during exposure and resist reflow during cure, perfectly vertical resist sidewall is difficult to achieve. Positive resists usually have a slightly positive slope, while negative resists have typically a negative profile. The comparison of positive and negative etch mask profiles are shown in Figure 13. Since the undercut of resist mask with negative profile can easily lead to the undercut and sloped sidewall of the final etch profile, positive profile is more preferable for etch masking. Commercial negative resist products are available which give positive profile. Thickness scaling down is a method to give maximum lithographic resolution. However the limited selectivity and mechanical stability restrict the resist application in many cases. Resists are simply not durable enough under harsh etch conditions such as aggressive chlorine plasmas. Harsh conditions also include long time and/or high temperature exposure to acid or base etchants. As a result, hard masks are utilized in many wet and dry etch processes.[4]

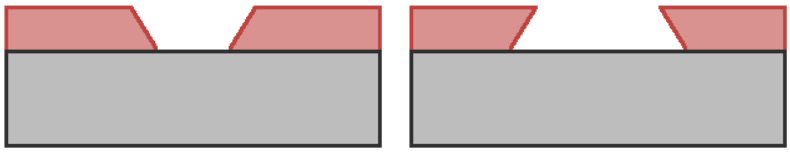

(a) (b)

Figure 13: The comparison of (a) positive and (b) negative etch mask profiles.

In silicon etching in KOH, silicon dioxide or silicon nitride are standard mask materials. In DRIE, many materials such as silicon oxide and aluminum can be used as hard mask. Aluminum nitride (AlN) and aluminum oxide (Al_2O_3) are very resistant in many plasmas, but can be easily etched in acid and base,[4] which gives flexibility for mask patterning and removal according to process integration. Vertical sidewall is also a preferable feature for hard mask. To get high aspect ratio structure, sometimes the mask is required to be patterned with RIE or DRIE. Scaling down the thickness is also a method to minimize the sidewall slope and roughness of hard mask.

2.3 Al_2O_3 as an etch mask for silicon

Selecting etch mask material is an important issue in DRIE of silicon. Hundreds micrometers or through wafer etch requires thick mask up to a few micrometers. For example, to etch a 350 μm deep hole with an area of 3 × 3 mm^2, utilizing $SF_6/CHF_3/O_2$ plasma, requires an aluminum mask of 100 nm.[22] However, patterning of a thick mask becomes nonfeasible when structure with sub-micrometer size is needed. With extremely high selectivity against silicon, Al_2O_3 is a promising candidate in this case. Additionally, Al_2O_3 possesses thermal and chemical stability, excellent dielectric properties and good adhesion to many surfaces, all of which make it a suitable mask material for DRIE of silicon.[23] Tegen et al. studied the etch characteristics of Al_2O_3 films for magnetically enhanced reactive ion etching (MERIE) and inductively coupled plasma (ICP) etching systems with the influence of bias power, source power and gas chemistry. The selectivities of Al_2O_3 to Si, Si_3N_4 and SiO_2 were investigated in various reaction conditions. When the reaction temperature was fixed at -15 ºC, variations of pressure, decoupled power and gas flow species were found to give a sufficient process window for profile control, uniformity over the wafer, etch rate, etc. The highest silicon to Al_2O_3 selectivity reached 69.7 in their study and the complete selectivity test results are shown in Table 2.[24]

Processing etchant	Si	Si_3N_4	SiO_2
Ar/CHF_3 3:1	1.5	4.8	4.8
Ar/CHF_3 2:1	2.0	5.3	5.5
Ar/CHF_3 1:1	2.1	5.2	4.8
CHF_3	4.8	11.1	9.0
Ar/CHF_4/0 sccm O_2	9.6	13.8	12.7
Ar/CHF_4/10 sccm O_2	8.3	10.5	8.5
Ar/CHF_4/20 sccm O_2	8.3	10.2	7.9
Ar/CHF_4/40 sccm O_2	7.2	9.5	6.9
50 sccm Ar/50 sccm CHF_4/10 sccm O_2	62.0	57.1	39.6
Ar/SF_6	19.7	9.2	5.4
SF_6	32.1	14.1	8.3
Ar/ Cl_2 (10 mTorr)	69.7	25.8	4.0
Ar/ HBr (20 mTorr)	8.7	1.4	3.9
CI/ Br	55.7	1.4	2.0
C_4F_6	0.85	2.6	17.2

Table 2: Selectivity of different materials to Al_2O_3 for various processes.[24]

In DRIE of silicon with Al_2O_3 mask, low temperature can help both to improve the silicon etching anisotropy and to decrease the etch rate of the mask. Grigoras et al. reported 1-5 nm thick ultra-thin Al_2O_3 masks grown by atomic layer deposition (ALD) on hydrogen-terminated silicon substrates for deep silicon etching at cryogenic temperatures in an ICP-RIE reactor. Al_2O_3 masks were patterned with photolithography and plasma etching. Results showed that 6 nm thick Al_2O_3 mask was sufficient for etching 400 µm into silicon when the process was conducted at -110 ºC, using SF_6/O_2 gas mixture. The etch rate of Al_2O_3 mask during silicon etching was found to be 0.05 nm/min, and the selectivity of silicon to Al_2O_3 reached 70000:1 in their research.[23]

Wet etching methods are available for Al_2O_3 and it can be carried out in both acid and base. This property is another merit of Al_2O_3 as a universal etch mask in microfabrication when wet etching is necessary for it. The chemical equations for the corresponding reactions are as follows:

$$2OH^- + Al_2O_3 \rightarrow 2AlO_2^- + H_2O \tag{3}$$

$$6H^+ + Al_2O_3 \rightarrow 2Al^{3+} + 3H_2O \tag{4}$$

The selection of Al_2O_3 etchant is related with the surface roughness requirement and the compatibility of other components on the fabricated wafer or chip.

Studies have shown that chemical reactivity of some amorphous materials are greater than that of the corresponding crystalline counterpart. It is reported that silicon, which is normally insoluble in acid, becomes soluble in dilute hydrofluoric acid after implantation

with argon or phosphorus as soon as the amorphization influence has been reached.[25] Single crystal Al_2O_3, or sapphire, is noted for its extreme resistance to attack by many chemical reagents. McHargue et al. reported that amorphous Al_2O_3 layer with enhanced chemical reactivity can be produced by ion beam irradiation of Zr, Cr, Sn or Al plus O.[26] It is also observed that gallium ions irradiated Al_2O_3 has a higher etch rate than non-irradiated Al_2O_3 in acid and base wet etchants.

The exact mechanism of the increased etch rate of Al_2O_3 upon ion implantation is not well established. The general consideration leading to this phenomenon is the structural change of Al_2O_3 upon ion implantation. Ions implanted into the Al_2O_3 lattice result in either temporary or permanent lattice distortions, depending on the implantation condition and foreign ion species.[27] Several mechanisms have been found, including formation of new phases from the initial lattice, local or global amorphization and precipitation of the implanted species.[28, 29, 30, 31, 32, 33] Besides, the introduction of additional ions into the lattice leads to an increase in volume, which subsequently, gives rise to compressive residual stress in the implanted layer.[34]

2.4 Atomic layer deposition (ALD)

Atomic layer deposition is an important thin film deposition technique in semiconductor processing due to its controllable deposition at atomic scale. Miniaturization of semiconductor devices requires atomic level control of thin film deposition and conformal deposition on very high aspect ratio structures. ALD meets the requirement for device scaling down by producing layers with nanometer scale thickness control, excellent conformity and wide area uniformity. Meanwhile, as conventional photolithography faces the resolution limit, device fabrication at sub-20 nm scale requires next generation patterning techniques such as electron beam lithography, focused ion beam and scanning probe based writing. However due to the slow process and high cost of these top-down processes especially for large scale production, bottom up approaches based on chemical synthesis and self-assembly process provide alternative processes besides lithography.

ALD was first introduced worldwide with the name atomic layer epitaxy (ALE) in the 1970s.[35] However as epitaxy is more commonly used in describing a growth of a single crystalline film on a single crystalline substrate with a well defined structural relationship between the two, ALE is not suitable to describe amorphous or polycrystalline film deposition. Other terms have been used to describe ALD include atomic layer growth, atomic layer chemical vapor deposition, molecular layer epitaxy, etc.

2.4.1 The principle of ALD

ALD is a special modification of chemical vapor deposition (CVD) with the distinct feature that film growth follows a pulsed mode. Figure 14 shows a normal growth cycle of a sequential self-limiting surface reaction during ALD. The first step is the exposure of the first precursor. The reaction continues until all the available reaction sites on the substrate surface are occupied. After that the the excess precursor gas and by-products

are purged out from the reaction chamber. Then the exposure of the second precursor takes place until the saturation of the first deposition layer, followed by a further purge of the reaction chamber. The growth cycles are repeated until the desired film thickness is reached. Most ALD processes are based on this binary reaction sequence that two surface reactions take place in order for binary compound film deposition.

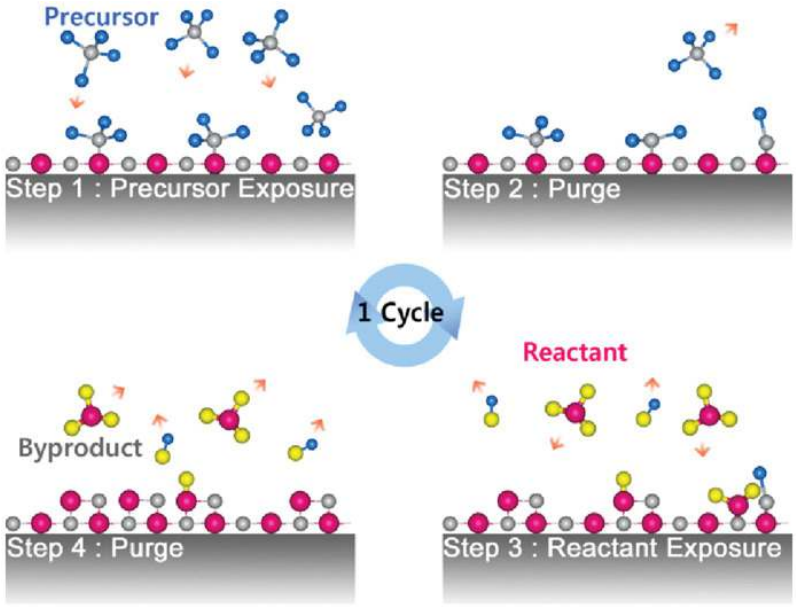

Figure 14: Schematics showing the growth process of ALD.[36]

One advantage of ALD is the precise thickness control at Angstrom or monolayer level. The self-limiting growth leads to excellent step coverage and conformal deposition on high aspect ratio structure. In theory, the ALD films remain extremely smooth and conformal to the original substrate since the reactions are driven to completion during every pulse. Because no surface sites are left behind during film growth, the films tend to be very continuous and pinhole-free, which is critical for the deposition of dielectric films. The substrate size for ALD is only limited by the reaction chamber dimension and parallel processing of multiple substrates is possible.

2.4.2 Al_2O_3 growth by ALD

The ALD of Al_2O_3 is usually performed with precursors trimethylaluminum (TMA) and water (H_2O). Other processes are also available for Al_2O_3 ALD with binary precursors such as TMA/ozone (O_3), TMA/hydrogen peroxide (H_2O_2) and aluminum chloride ($AlCl_3$)/H_2O. The TMA/H_2O process is considered an ideal model for ALD because the reactants are highly reactive, but at the same time thermally stable, and the gaseous reaction product, methane, does not interfere with the growth.[37]

The TMA/H_2O process that follows the overall stoichiometric reaction is shown in Equation 5.

$$2Al(CH_3)_3 + 3H_2O \rightarrow Al_2O_3 + 6CH_4 \quad (5)$$

The chemical reaction of TMA/H_2O process is often described by two successive half reactions as follows:

$$Al - OH^* + Al(CH_3)_3 \rightarrow Al - O - Al(CH_3)_2^* + CH_4 \quad (6)$$

$$Al - CH_3^* + H_2O \rightarrow Al - OH^* + CH_4 \quad (7)$$

where the asterisks indicate the surface species. By repeating the surface reactions, the Al_2O_3 film thickness is extremely linear with the number of binary pulses. Typical measured Al_2O_3 ALD growth rates are 1.1-1.2 Å per binary pulse.

2.4.3 Compound and single element ALD materials

ALD is closely related to CVD based on binary reactions which produce compound materials. ALD reactions with negative reaction heats which can take place spontaneously at various temperatures are referred to thermal ALD because they can be performed without the aid of plasma or radicals. Most thermal ALD reactions produce binary compounds based on binary reactant CVD. The most common materials deposited by thermal ALD are binary metal oxides such as Al_2O_3, TiO_2, ZnO, ZrO_2, HfO_2 and Ta_2O_5. Other common thermal ALD materials are binary metal nitrides such as TiN, TaN and W_2N. Thermal ALD processes are also available for sulfides such as ZnS and CdS and phosphides such as GaP and InP.[38]

Single element materials such as metals and semiconductors that can not be deposited by a binary reaction sequence can be deposited using plasma enhanced ALD. With the aid of energetic species in the plasma such as radicals, deposition reaction can take place when bare thermal energy is not sufficient. Hydrogen radical enhanced ALD can be used to deposit titanium (Ti), tantalum (Ta), silicon (Si) and germanium (Ge). Plasma enhanced ALD can also be used for compound deposition, which allows low temperature deposition. Metal ALD can also be accomplished using thermal reactions without plasma enhancement. The main types of metal ALD using thermal chemistry are based on fluorosilane elimination, combustion chemistry or hydrogen reduction.[38]

2.4.4 ALD applications in microelectronics

2.4.4.1 Electroluminescent display phosphors ALD was originally developed for thin film electroluminescent (TFEL) displays in the middle of the 1980s. ZnS:Mn has been found to be the most efficient TFEL phosphor emitting light in the yellow to orange range. No major difference in luminescence can be found between the ALD and other techniques deposited films.[39] A clear advantage of ALD is the large grain size at the beginning of the film growth which ensures that in ALD films

the dead layers with no emission are thinner than in the films deposited with other techniques.[40, 41] ZnS:Tb is another zinc sulfide-based material that has sufficient electroluminescent properties for phosphorescence applications. Additional to depositing the active dielectric-phosphor-dielectric stack, ALD can be used to deposit a pinhole-free ion barrier layer on a soda lime glass substrate and as a passivation layer on top of the device structure.[35]

2.4.4.2 High permittivity (high-$\varkappa$) dielectrics The continuous device dimension scaling in the integrated circuits requires the scaling of dielectric materials. In both metal oxide semiconductor field effect transistors (MOSFETs) and dynamic random access memory (DRAM) capacitors, scaling of silicon based insulator such as silicon dioxide (SiO_2) and silicon oxynitride (SiO_xN_y) stopped at thickness close to 1.0 nm due to the detrimentally high tunneling currents. Insulators with high-$\varkappa$ and corresponding deposition methods in good control are expected to solve this problem. A convenient measure for the dielectric material capacitance density is the equivalent oxide thickness (EOT) which is expressed as

$$EOT = d_{high-\kappa}\kappa_{SiO_2}/\kappa_{high-\kappa} \tag{8}$$

in where κ_{SiO_2} is the dielectric constant of SiO_2, $\kappa_{high-\kappa}$ is the dielectric constant of the high-$\varkappa$ dielectric material and $d_{high-\kappa}$ is the physical thickness of the high-$\varkappa$ layer. The current trend of device fabrication is to have EOT under 1.0 nm.[42] ALD possesses distinctive advantages for high-$\varkappa$ material deposition because it enables very thin film deposition with accurate thickness control over large areas. Additionally, in DRAM capacitor applications excellent conformality is particularly appreciated due to the three dimensional memory capacitor structures.

2.4.4.3 Transparent conductors Transparent conducting oxides (TCOs) have a wide range of applications such as in flat panel displays, solar cells, light emitting diodes and antistatic coatings. Indium tin oxide (ITO), the current dominant transparent conductor for electronic devices is not likely to satisfy future needs due to the limitation of the element indium in the earth. Besides, ITO also has other disadvantages, such as brittleness, instability in the presence of acid or base and limited transparency in the near infrared region. ALD processes have been developed for many TCO materials such as zinc oxide and tin oxide, which provides potential alternatives for ITO. ALD is an attractive method for TCO deposition due to the superior uniformity, conformality and compactness of the achieved film compared to other techniques. It also allows low temperature deposition, for example ZnO:Al growth at 120-350 °C.[43] Besides, TCOs are quite often doped materials for improved property. ALD also gives the ease for doped material deposition by switching a fraction of deposition cycles to precursor containing a dopant.

Zinc oxide (ZnO) is a promising alternative for ITO and has received great attention in recent years. Conductivity of ZnO can be increased by doping with n-type trivalent atoms such as boron, aluminum, gallium and indium. A recent research shows that sheet resistance reaches 25 Ω/□ for a 575 nm thick aluminum doped ZnO film grown

by ALD at 325 °C, followed by annealing at 400 °C in argon ambient. At the same time the film has 80-90% transmittance in the visible region.[44] Transmittance over 70% is observed for the above mentioned ZnO film in the mid-infrared region until 2500 nm wavelength, which is comparable to that of a 150 nm ITO film prepared by activated reactive evaporation.[45]

Major drawback of ALD is the low growth rate compared to sputtering systems. For example, effective growth rates up to 13 nm/min are achievable for doped ZnO, which is barely comparable to RF sputtering systems with growth rates of 15-20 nm/min.[46] In contrast, ZnO growth rate is around 300 nm/min for dual magnetron sputtering.[47]

2.4.4.4 Passivation and diffusion barriers ALD technique has also been used for passivation and diffusion barrier materials deposition. Due to the surface controlled self-terminating gas-solid reaction, ALD enables the preparation of dense and pinhole-free films which are uniform in thickness even deep inside pores, trenches and cavities of various dimensions. Other advantages of ALD include low impurity content and wide process window in deposition temperature and/or pressure.

The first application for diffusion barrier purpose is to use ALD Al_2O_3 as an ion barrier layer in TFEL displays.[35] The sodium out-diffusion from soda lime glass prevents this inexpensive glass from being used as a substrate in devices sensitive to sodium. It has been proved that Al_2O_3 films prepared by ALD effectively prevent the sodium migration,[48] which facilitates the soda lime glass application instead of more expensive near-zero alkali glasses. The excellent conformality and amorphous structure with no grain boundaries are the key benefits of ALD Al_2O_3 films in blocking the migration of ion, gas and moisture.

As the continuous miniaturization of electronic devices, the cross sections of metal lines have decreased accordingly. Consequently the thickness of diffusion barrier, which inserts between metals and surrounding silicon or insulator and prevents metal diffusion, has to be adapted according to critical dimensions and loss of conductivity. As projected by the International Technology Roadmap for Semiconductors, the allowable thickness of the next generation devices is expected to be around 2 nm for the 25 nm technology node by the year 2015.[49] At the same time, the aspect ratio of trenches and vias has increased. According to these trends, ALD provides distinguished benefits for diffusion barrier deposition. A few nanometers thick film can be deposited uniformly all around the deep trenches and vias, and still has void-free structures to effectively prevent the detrimental interactions. Transition metal nitride layers such as TiN, TaN, $Ta_xSi_yN_z$ and $W_xSi_yN_z$ have been developed as diffusion barriers. Another promising candidate is tantalum oxide (Ta_2O_5) which is amorphous and possesses high chemical and thermal stability. Lintanf-salaün et al. demonstrated the application of ALD Ta_2O_5 as diffusion barriers for microelectronic devices. As shown in Figure 15, good conformity was observed for a 20 nm thick film deposited on both planed and patterned substrates in their study. Film remained amorphous and provided good barrier for copper after 1 hour heat treatment at 600 °C.[50]

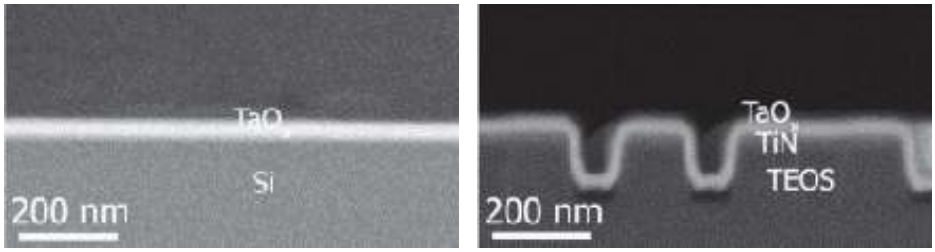

(a) (b)

Figure 15: Field effect scanning electron microscope images of cross sections of 20 nm thick tantalum oxide layer deposited by ALD on (a) planed and (b) patterned silicon substrates.[50]

2.5 Ion implantation

Ion implantation is a technique using energetic ion beam to introduce ions into a substrate. This process changes the physical, chemical and/or electrical properties of the target solid. Ion implantation was first applied to semiconductor as a means of introducing controllable concentrations of n- and p-type dopants at precise depths below the surface.[51] Accelerated ions hit the silicon wafer, penetrate into silicon, slow down by collisional stochastic processes and come to rest within femtoseconds. Due to the flexible dopant selection, capability of ion spacial injection and subtle concentration control, ion implantation has replaced thermal diffusion almost completely in complementary metal oxide semiconductor (CMOS) fabrication and become the main method to introduce dopants into silicon. Typical ion implantation energies range from 10 keV to 200 keV, and doses range from 1×10^{11} ions/cm^2 to 1×10^{16} ions/cm^2. Ion implantation depths are of the order of hundreds nanometers, thus the corresponding concentrations are approximately 10^{15}-10^{20} ions/cm^3. Crystal damage removal and dopant activation should be followed by implantation and can take place simultaneously during a thermal anneal.[4]

2.5.1 Ion-surface interaction

During ion implantation, energetic dopant ions are made to impinge on the silicon or other target, resulting in the penetration of these ions below the target surface which gives rise to controllable and predictable dopant distribution. Foreign ions alter the elemental composition of the substrate, and also cause chemical and physical change of the target by transferring their energy and momentum to the electrons and atomic nuclei of the target material. A quantitative understanding of the atomic interactions between these energetic ions, target atoms and masking layer is necessary for the prediction of the depth and lateral doping profiles produced by ion implantation process. These interactions depend on the relative mass of ion and target atom, ion energy, ion angle of incidence and target crystal orientation and perfection. Ion-atom interactions during ion implantation can cause collateral damages including vacancy, interstitial, vacancy cluster, interstitial

cluster, dopant-interstitial and dopant-vacancy cluster and local amorphization of crystal target.

It is well established that energetic ions are decelerated in the lattice to a halt through electronic stopping and nuclear stopping. The former is the interaction between electronic clouds of the target and projectile ion and the later is the atomic collision between the projectile and target atoms. The statistical distribution of the stopping points for implanted ions constitutes a concentration versus depth profile. The prediction of such doping profiles is a central issue that underlies the interest in the stopping process. Stopping is characterized by an energy loss per unit length of travel, which is described as

$$\frac{dE}{dx} = S_n(E) + S_e(E) \tag{9}$$

where $S_n(E)$ and $S_e(E)$ are respectively the nuclear and electronic stopping components, both of which are a function of the ion energy, atomic number, atomic mass, as well as the target atomic number, atomic mass and packing density. The ion range is resulted from the apportionment of the incident projectile energy over these stopping components.

Electronic stopping is inelastic and results in electronic states decay of the excited target without producing atomic displacements. Nuclear stopping is elastic and is caused directly by atom displacement and disorder. In semiconductors, only elastic collisions usually generate lattice damage, while in insulators both processes can induce atomic displacement. During nuclear stopping, momentum and energy transfer between the projectile and target atoms, which may result in the generation of energetic knock-on target atoms. This process may continue and produce secondary, tertiary and higher order knock-on displacements, which results in a damage chain, known as a collision cascade. Collision cascade leaves behind defects such as substitutions, interstitials and vacancies.

Electronic stopping is similar to dragging a particle in a viscous medium, and involves both target and projectile electron excitation. It may also involve electron capture or loss from the bound states of the moving projectile ion. These processes determine the charge state and effective electronic stopping power of the ion when it moves through the solid. At high velocities when $v \gg Z_1 v_0$, where Z_1 is the ion atomic number and v_0 is the Bohr velocity = 2.2×10^8 cm/s, the ion strips off its bound electrons. In this case stopping can be calculated using the Bethe-Bloch theory. Such stopping is rarely encountered in ion implantation since even lightest ions typically have velocities in the range of $0.1v_0$ to $5v_0$. At low velocities when $v < v_0$, such as which are typically encountered in the energy range of 2-400 keV, the projectile ions are essentially neutral and stopping is proportional to the ion velocity according to the equation:[52]

$$S_e(E) = k_e(E)^{\frac{1}{2}} \tag{10}$$

The stopping power proportionality constant k_e is a periodic function of the atomic number of the projectile ion.

Equation 10 is no longer valid when the projectile velocity approaches the average orbital electron velocity $v \approx Z_1^{\frac{2}{3}} v_0$, since the projectile starts partially stripping off some electrons.

In this case the stopping power is determined through proportion with the known stopping of a proton in the target at the same velocity through a proportion constant Z_1^*, known as the stopping power effective charge:[53]

$$(Z_1^*)^2 = S_{Z_1}/S_p \tag{11}$$

where S_{Z_1} is the desired stopping power of the partially stripped ion, S_p is the proton stopping power. Z_1^* depends on the degree of ionization of the projectile, degree of inter-penetration of the target electrons and the remaining bound electrons moving with the projectile. Z_1^* is therefore greater in magnitude than the degree of ionization. The solution of the stopping problem involves firstly to determine the velocity dependent degree of ionization, and then based on this to calculate the stopping power effective charge Z_1^*.

In most nuclear stopping models nuclear stopping is treated as a binary collision between the target and projectile particles. The presence of other atoms in the crystal lattice is taken into account through the interaction potential between target and projectile ions, a displacement energy, a binding energy and the above described electronic stopping processes. This approach is valid over a wide range of ion energies. This approach does not apply for low energies (< 5 keV) and a more general Molecular Dynamics scheme is required for broadly calculating the interactions with the ions and the ensemble of nearby target atoms. These methods involve extremely intensive computation. Figure 16 depicts the binary collision that results in nuclear stopping when projectile ion with mass M_1 approaches the target atom with mass M_2. The path of the projectile ion is offset from the center of the target atom by impact parameter p. A value of $p = 0$ implies a head-on collision, whereas non-zero values of p imply a glancing blow. When $p > r_1 + r_2$, in where $r_1 + r_2$ indicates the respective atomic radii, the projectile ion misses the target atom and no collision occurs. The projectile ion approaches the target atom with velocity v_p, and moves off with velocity v_1 after colliding, deflecting through an angle α with respect to its initial moving direction. The target atom acquires velocity v_2 , deflecting through an angle β with respect of the projectile incoming direction. Energy conservation requires $v_1 \leq v_p$, that the initial kinetic energy of the projectile is no smaller than the post-impact kinetic energy. The projectile energy loss is directly related to the impact parameter and interaction potential during a collision. Thus the determination of nuclear stopping requires known interaction potential value and the deflection angles assumed by impact parameter.[54]

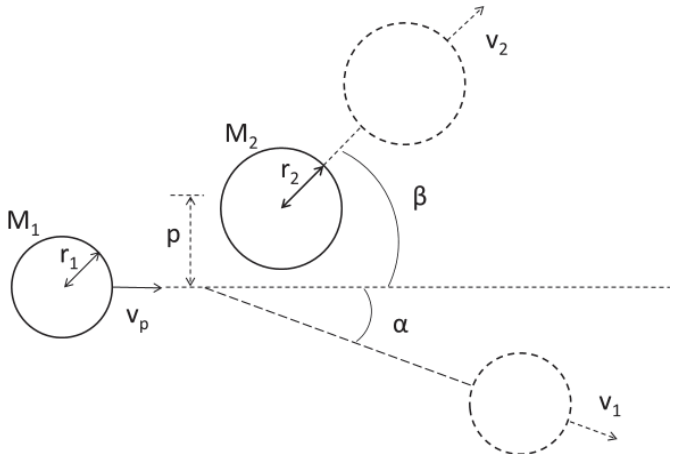

Figure 16: Schematic illustration of a binary collision between a projectile with mass M_1 and initial velocity v_p and a stationary target atom with mass M_2.

The relationship between energy transfer and deflection angle is most conveniently determined with a center of mass coordinate system. The interaction potential is dependent on the screening effect of the surrounding electrons of the target and projectile nuclei, and the quantum mechanical interactions between their overlapping electron clouds. Various approximations of these interactions have been attempted, and the most accurate methods involve Hartree-Fock models of the atom. Such calculations are computation intensive, and are used primarily as benchmarks to establish accurate simpler approaches.[54]

2.5.2 Ion implantation simulation

Analytical and the Monte Carlo simulation are the two methods which are commonly used in ion implantation simulation. The increasing accuracy requirement due to the continued device dimension downscaling necessitates the transition from the simple analytical ion implantation simulation to the particle-based Monte Carlo simulation for more and more applications.

The basic idea of the analytical approach is that the doping profile can be approximated by a statistical distribution function. This function depends on a set of parameters which can be expressed by characteristic parameters of the implanted dopant distribution. The characteristic parameters, the so-called moments, can be extracted from Monte Carlo calculation results or from measured doping profiles. One-dimensional distribution functions can be combined to multi-dimensional profiles by a convolution method which takes into account a dose matching rule and numerical scaling. The analytical simulation of ion implantation profiles requires relatively short computing time, even in two- and three-dimensions.

Back in 1960s, Lindhard et al. combined the effects of nuclear and electronic stopping to achieve an analytical way to predict the statistical distribution of a large number of implanted ions. They acquired a general analytical solution to Equation 9, by

approximating that the ion velocity dependent electron stopping obeys Equation 10 and nuclear interaction potentials are derived from the Thomas-Fermi model of the atom. This research yields mean range R and standard deviation of ranges called straggle ΔR_p. The mean range determination also allows the determination of mean projected range R_p, which is the mean distance below the target surface in the direction determined by the initial incidence trajectory of the projectile ion. The final ion distribution profile is then determined by assuming a Gaussian distribution with the mean value R_p, and standard deviation ΔR_p.[55] This model applies to amorphous targets only, and does not give sufficiently accurate results for semiconductor device simulation. However, this model is crucial for stopping physics state advancing and it is still a common practice to approximate implantation profiles by Gaussian approximation, using R_p and ΔR_p determined by alternative means. The Gaussian depth-concentration profile is determined from Equation 12:

$$n(x) = \frac{\phi}{\sqrt{2\pi R_p}} \exp\left[-\frac{(x-R_p)^2}{2\Delta R_p^2}\right] \tag{12}$$

where ϕ is the important dose in atoms/cm^2. The peak concentration for such a distribution is given by Equation 13:

$$n(x = R_p) = \frac{\phi}{\sqrt{2\pi}\Delta R_p} \cong \frac{0.4\phi}{\Delta R_p} \tag{13}$$

Current methods of profile prediction using Monte Carlo simulation are computation intensive. Very accurate results can be yielded with appropriate selection of electronic and nuclear stopping algorithms. They imitate the implantation process by computing a large number of individual ion trajectories in the target. The result of this model is used to describe the implantation profile as a statistical distribution function. Since the Gaussian distribution is described by only two moments, the mean and the variance, it is usually inadequate for such fitting. Accurate profile description requires four moments involved, which are mean range, variance, skewness and kurtosis. With suitable fitting, Monte Carlo method is able to simulate the channeling effect and accumulation of point defects during implantation in crystalline targets, as well as shadowing effects arising from mask edges, etc. The underlying physical models are applicable for a wide range of implantation conditions without additional calibration.[54]

A number of Monte Carlo simulation codes relied on binary collision approximation (BCA) have been developed since the mid-1970s to compute sputter yields in addition to implantation depth and other relevant quantities. Monte Carlo simulation programs such as TRIM/SRIM, MARLOWE, UT-MARLOWE, TRIRS, DYTRIRS and FIBSIM provide significant insight into the physics of implantation process. These programs model projectile-target interactions and target-target interactions as a series of two-body interactions. Programs such as TRIM are limited to amorphous target materials which do not simulate the channeling tail very accurately. On the other hand, Monte Carlo simulators such as UT-MARLOWE are based on the crystal structure of the substrate. Polycrystalline samples can also be approximated to single crystal structures.

Transport of ions in matter (TRIM) is one of the most widely used simulation programs for ion implantation and ion beam processes due to its fast treatment of a large number of projectile ions. Stopping and range of ions in matter (SRIM) is a group of computer programs which calculate the stopping and range of ions (10 eV/amu-2 GeV/amu) into matter with the core of TRIM. TRIM accepts complex targets made of compound materials with up to eight layers and each layer material differs from others. It calculates both the final 3D distribution of the ions and also all kinetic phenomena associated with ion's energy loss including target damage, sputtering, ionization and phonon production. All target atom cascades in the target can be followed in detail. It can be used for physics of recoil cascades, physics of sputtering, the stopping of ions in compounds and stopping powers for ions in gases, including radiation damage from neutron, electron and photon.

Like all BCA codes, TRIM models the collision cascade as a series of binary collision events between a moving atom and a stationary atom. In each event, the impact parameter is chosen in a stochastic manner and the energy transfer in the collision is computed. Once the energies of two atoms are known, their energies are compared to the following parameters: displacement energy E_d, binding energy of an atom to its site E_b, the surface binding energy E_s and final energy E_f after which the atom is no longer traced. If the energy of the originally stationary atom after collision E_2 is higher than the displacement energy E_d, then the atom is dislodged from its site and continues to travel with energy $E_2 - E_b$. Otherwise, the stationary atom will dissipate its energy as phonons. Similarly, if the energy of the originally moving atom after the collision E_1 is higher than E_d, the moving atom also continues to collide and a vacancy is created. If E_1 is lower than E_d, the initially moving atom takes place of the initially stationary atom, resulting either a replacement collision when the involved atoms are of the same kind or an interstitial defect. When replacement collision or interstitial takes place, the excess energy is assumed to dissipate via phonons. In the case that both E_1 and E_2 are lower than E_d, the initially moving atom becomes an interstitial defect and all the energy is released as phonons. When an atom is given sufficient energy that its kinetic energy normal to the surface exceeds the surface binding energy of the target material E_s, the atom can sputter across the surface.

The results of TRIM simulation are highly dependent on the potential used to calculate the collision events and various energetic parameters selected. Many of these parameters are known only for a small amount of possible targets. The sputtering yield is particularly sensitive to the surface binding energy and lattice binding energy. While the former is usually approximated to the heat of sublimation, and the later is not explicitly known for most compounds. In addition, TRIM program can not take into account the surface roughness and surface stoichiometry change which may occur during sputtering.

2.5.3 Ion implantation applications

Ion implantation emerged in the 1960s as a means of introducing controllable concentrations of n- and p-type dopants at precise depths below the surface. It is an essential process in modern IC manufacturing. The most commonly implanted species include arsenic, phosphorus, boron, boron difluoride, indium, antimony, germanium, silicon, nitrogen, hydrogen and helium. Ion implantation excels over thermal diffusion in semiconductor industry due to its advantage in precise, reliable and repeatable control of dopant deposition. Ion implantation applies to shallow doped structure formation, such as piezoresistors on atomic force microscope (AFM) cantilevers, advanced CMOS source/drain diffusion and bipolar emitter regions diffusion. Some typical applications for ion implantation are listed in Table 3.[56]

Application	Substrate	Ion	Doped area
Doping of semiconductors	Si	B^+	p-Si
Generation of buried insulating layers	Si	O^+	SiO_2
	Si	N^+	Si_3N_4
Production of compound semiconductors	Si	C^+	SiC
Production of conducting silicides	Si	Co^+	Co_2Si
Generation of insulating layers in metals	Al	N^+	AlN

Table 3: Typical applications of ion implantation.[56]

2.6 Focused ion beam (FIB) technology

FIB systems have been produced commercially for 20-30 years.[57] An FIB process involves the bombardment of the specimen surface by extracted ions from ion source, usually liquid metal ion source (LMIS), which results in not only ion implantation but also amorphization, sputtering and secondary electron and ion generation. The controllable FIB position allows maskless direct patterning pixel by pixel. The secondary ions and electrons generated as the beam scanning over a sample can be utilized for imaging and sputtering enables specific feature machining or modification. Beside material removal function, FIB systems can be equipped with a gas injection system which is used for material deposition.

2.6.1 FIB system introduction

The main components of FIB system include ion column, work chamber and vacuum system. The latest models which are called dual platform systems combine both ion and electron beam columns. The electron column enables navigation over a sample and monitoring of the FIB milling in real time, thus eliminates sample damage by FIB imaging. In single beam FIB systems, an FIB ion column locates on the top of the specimen chamber. Alternatively in dual beam systems, the SEM column is on the top of the chamber and the FIB column is inclined at an angle of 45°-52° to the SEM

column as shown in Figure 17. The schematic presentation of a typical FIB ion column is shown in Figure 18. The structure of the column is similar to that of a scanning electron microscope, and the main difference lies in that usually a gallium ion (Ga^+) beam is used instead of an electron beam. The LMIS mounts on the top of the column from which the beam of ions is field extracted. Beneath LMIS are a series of lenses and apertures which collimate and focus the ion beam. The LMIS typically consists of a tungsten needle with a radius of curvature of 1 µm which is wet by a liquid metal. Typically gallium is used as LMIS for the following reasons. Firstly it does not form an alloy with tungsten needle. Secondly gallium has a low melting point 29.8 ℃ which avoids excessive heating of the ion column. Besides the low vapor pressure makes gallium suitable for high vacuum process. Additionally the high ration of gallium ions in the ion source gives a narrow energy distribution of the ion beam.

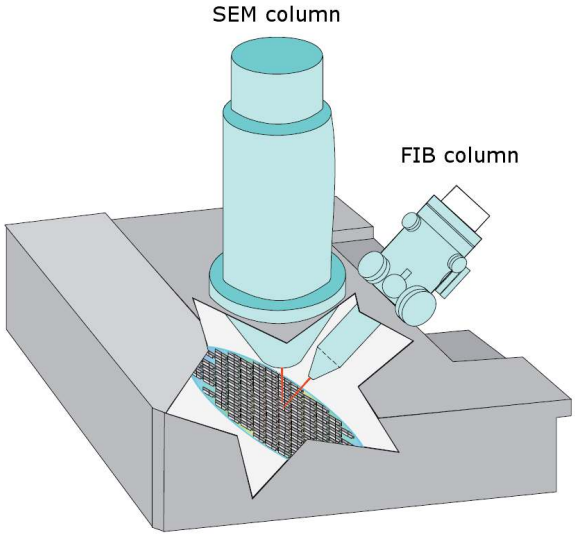

Figure 17: Schematic illustration of SEM and FIB columns in a dual beam FIB system.[57]

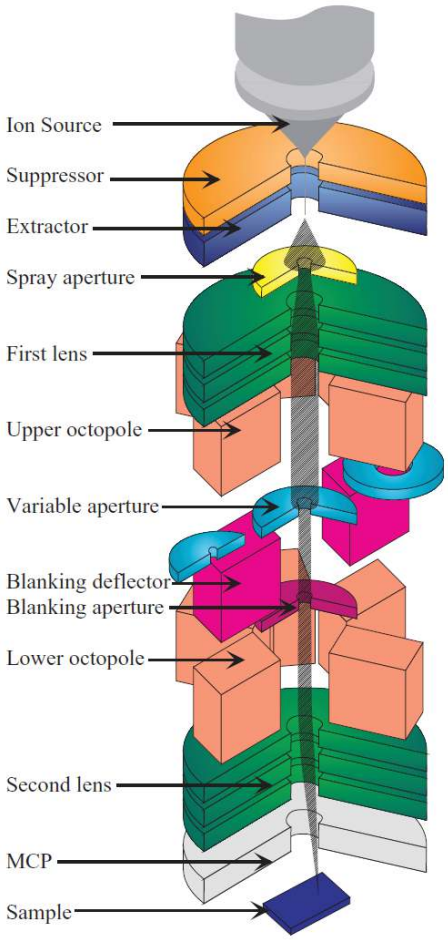

Figure 18: Schematic illustration of a typical FIB ion column.[58]

The ion beam is generated from the LMIS by applying a strong electric field. When a large potential gradient at the magnitude of 10^{10} V/m is applied to the wet tip, a Taylor cone with radius of curvature around 10 nm is formed through a balance between electrostatic forces and surface tension. The resulting large field at the cone apex lowers the potential barrier and enables field extraction. The emission current, usually 1-3 μA, is then accelerated typically to 30-50 kV. Coulombic interactions between the ions result in a virtual spot size of approximately 50 nm at the source.[57]

The ion distribution of an FIB can be approximated to a Gaussian distribution. The schematic ion beam intensity distribution curves with different currents are shown in Figure 19. Due to that the ion intensity is highly non-uniformly distributed, the full width at half-maximum (FWHM) is commonly used to describe the FIB spot size. The FWHM is defined as the distance between the locations on the intensity profile at which the intensity reaches half of its maximum value. The beam size can be controlled by varying the beam current and a lower current leads to a narrower beam. Using the variable aperture mechanism, the beam current can be varied over four decades, allowing both fine beam for high resolution imaging on delicate samples and heavy beam for fast and rough milling. Due to lens aberrations (spherical and chromatic) and space charge effects, the

smallest spot size when the beam current is 1-5 pA is limited in the order of 5-10 nm. As the magnitude of beam current increases, the spot size increases correspondingly. For example, at 20 nA beam current, the spot size is of the order of 200 nm. The FWHM definition and the comparison of FWHM dimensions when beam current varies are also schematically shown in Figure 19.

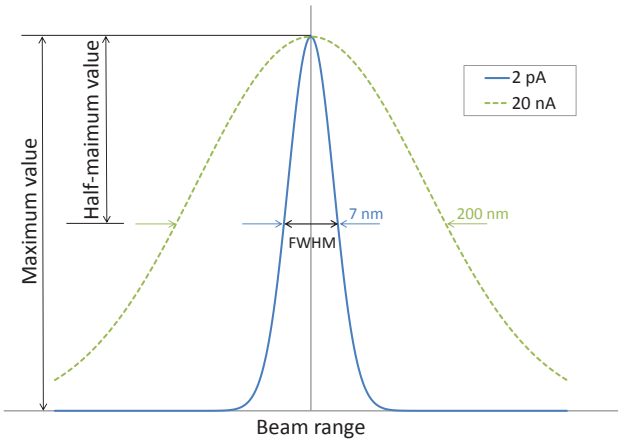

Figure 19: Schematic drawing of different FIB intensity distribution curves and the illustration of FWHM of the solid line. Graph dimensions are not in scale.

2.6.2 Principles of FIB imaging, milling, deposition and implantation

The FIB can be scanned using electrostatic deflection plates, pixel by pixel over the surface of a sample, while the dwell time can be varied. The number of gallium ions incident per unit area indicates the ion dose. At doses lower than 10^{14} ions/cm^2, the process is ion implantation and at higher doses it is referred to as sputtering.[57] When energetic ions hit the surface of a solid sample they lose energy to the electrons of the solid as well as to its atoms. The most important physical effects of incident ions on the substrate and the corresponding functions are listed in Table 4.

Physical effect	Resulting function
Sputtering of neutral and ionized substrate atoms	Substrate milling
Electron emission	Imaging (Sample may be charged.)
Displacement of atoms in the substrate	Induced damage
Emission of phonons	Heating

Table 4: Physical effects and corresponding resulting functions of incident ions on a sample in FIB systems.

Ion beam scanning on the specimen surface results in the emission of atoms, secondary

ions (SIs) and secondary electrons (SEs). As shown in Figure 20a, the SIs and SEs can be collected on a biased detector for imaging similarly to SEM. The detector bias is positive or negative respectively, for collecting SEs or SIs. The emitted SIs can be used for secondary ion mass spectroscopy (SIMS) of the target material in a mass spectrometer attached to the system.

During FIB imaging, it is inevitable that a small amount of Ga^+ ions are implanted in the sample and a large number of SEs leave in the sample. To prevent positive surface charges building up, the substrate can be flooded with electrons from a separate electron source. The system thus prevents the damage due to electrostatic discharge and enables the reliable imaging of non-conducting materials such as glass.

The highest ion image resolution is of the order of 5-10 nm for a 1-10 pA beam which is one order less than what can be achieved by a field emission scanning electron microscope.[57] Contrast in an FIB SE image can be affected by topography, atomic number and ion channeling. In ion channeling the beam passes down a zone axis and dissipates the energy further away from the surface. As a result, the generated ions and electrons have a higher probability of dissipating the energy through collisions before they reach the surface. Topography contrast originates from the greater cascade volume close to the sample surface which increases the probability of secondary electron escaping.

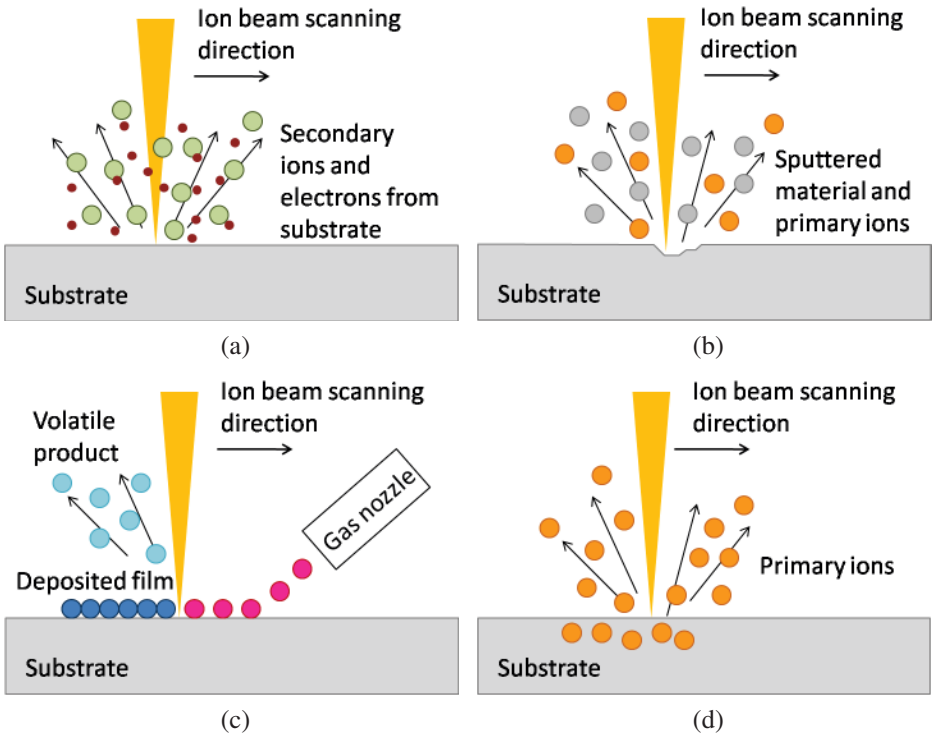

Figure 20: Schematic illustration of FIB operation principles: (a) imaging; (b) milling; (c) deposition and (d) implantation.

FIB can also be used for material milling. As illustrated schematically in Figure 20b, the removal of sample material is achieved by using a high ion current beam which results in

the physical sputtering of sample material. Arbitrary shape can be fabricated by scanning the beam over the substrate. Typical sputtering yield features with normal incidence for various materials are shown in table 5. It should be noticed that these values cannot be used directly for etch rate calculation because redeposition can drastically reduce the effective etch rate. Besides, the sputtering yield is also dependent on the angle of incidence.

Ga^+ ion energy (keV)	Implantation depth (nm)			Sputtering yield (atoms/ion)		
	Si	SiO_2	Al	Si	SiO_2	Al
10	13 ± 5	12 ± 4	11 ± 4	1.46	Si: 0.62; O: 2.23	2.59
20	20 ± 7	19 ± 6	17 ± 6	1.87	Si: 0.64; O: 2.24	2.98
30	27 ± 9	25 ± 8	23 ± 8	1.98	Si: 0.67; O: 2.25	2.91
40	33 ± 11	31 ± 10	29 ± 10	2.04	Si: 0.77; O: 2.54	3.54
50	39 ± 14	38 ± 11	35 ± 12	2.01	Si: 0.67; O: 2.29	3.48

Table 5: Typical implantation depths and sputtering yields for Ga^+ ions in Si, SiO_2 and Al at normal incidence calculated from TRIM Monte Carlo simulation.[59]

The smallest ion beam spot size is of the order of 10 nm which enables corresponding dimension features to be patterned. This feature size is comparable to the line widths of 10 nm that can be achieved by lithographic methods such as nanoimprint and electron beam lithography.

FIB can also enable localized maskless deposition of both metal and insulator in user-defined patterns. The most common metals that can be deposited in commercial FIB systems include platinum (Pt) and tungsten (W). The most common FIB deposited insulator is SiO_2. In addition, other metals such as gold (Au) and Cobalt (Co) have also been deposited. The principle of beam-assisted deposition is shown in Figure 20c. A suitable precursor gas, for example methylcyclopentadienyl(trimethyl)platinum for Pt deposition, is bled into the vacuum system usually via a needle which is inserted close to the sample and the beam. The precursors are sprayed on the surface and broken down by the SE. Then the volatile reaction products desorb from the surface and are removed through the vacuum system, while the desired reaction products adhere to the surface as thin film. The deposition material is not fully pure since organic contaminants as well as Ga^+ ions are inevitably included.

The deposited line widths are influenced by many factors, such as the gas flux, thickness and applied beam energies. Typical features that can be deposited for 60 nm thick lines are of the order of 60 nm width.[57] Aspect ratios between 5 and 10 are obtained, at a typical deposition rate of 0.05 $\mu m^3/s$.[58]

Ion implantation is impeditive but unavoidable during FIB imaging and machining processes. Nevertheless, ion implantation by FIB provides particular advantages for maskless material surface modification. As shown in Figure 20d, a specific mass of ionized atoms from the ion source are used in FIB implantation. The accelerated ions bombard the surface of the substrate with high kinetic energy and are implanted.[60]

In the course of an FIB process, imaging, milling and ion implantation always take place at the same time. The selection of dwell time, ion beam current and dose determines which one is the dominant outcome.

2.6.3 FIB applications in micro- and nanofabrication

FIB and dual beam systems, for example systems with both ion and electron beam columns, have been extensively used for micro- and nanofabrication during the past 10-15 years, for example, for circuit modification[61] and read-write head trimming[62]. As introduced above, FIB systems can sputter and implant lines as narrow as 10 nm and deposit metals and insulators down to 10 nm in user-defined patterns. In addition, during the FIB scanning, signals such as generated SEs can be collected for imaging. The combination of these functions gives the FIB system great variety of applications in micro- and nanofabrication. The applications typically fall into two categories. One category is the fabrication or modification of structures and devices that are difficult to prepare by conventional techniques due to material or geometry restrictions. For example, FIB can be used to pattern materials such as chalcogenide glass,[63] for which the wet or dry etching chemistries are complicated or unclear. Lacour et al. also reported the fabrication of FIB patterned periodic structures into $LiNbO_3$ film which is difficult to fabricate by wet etching.[64] Another category is the rapid prototyping or modification of structures which takes more and more complicated steps by conventional processing. An example is the quick connection of nanowires and carbon nanotubes dispersed on pre-patterned electrodes and contact pads with the dimension within 20 μm. In situ ion and electron beam-assisted deposition can be used to contact nanowires and carbon nanotubes to the electrodes within 30 minutes. In contrast, using electron beam lithography and metal lift-off process can take up to two days.[65]

2.6.3.1 FIB milling FIB milling is the most commonly used application of the system and has been used to prepare a wide rang of devices including lenses on fiber ends, pseudo spin valves, pillar microcavities and stacked Josephson junctions.

FIB 2D patterning into dots, lines and arrays can be used for a wide range of materials. 2D pattern densities achieved by FIB milling are comparable to electron beam lithography. Arrays of circles or squares with down to 40 nm feature sizes and spaces can be routinely prepared by both techniques. Due to the tails of the ion beam profile may sputter away the material between the elements, FIB milling for features smaller than 40 nm is challenging. In addition, metal lift-off step also becomes difficult in electron beam lithography for features smaller than 40 nm for the similar property of electron beam.[65] Despite of the similar sufficiency of FIB milling and electron beam lithography in microfabrication, FIB milling is more preferable in some processes. One example is the reduce of the handling required in the case of fabricating structures on membranes. Such membranes are very fragile and can be easily broken during resist application and metal lift-off step required for electron beam lithography. Enkrich et al. utilized FIB rapid prototyping for sub-wavelength split-ring resonator (SRR) design and feasibility test. Due to the time-consuming dose test and processing steps required for this sort

of SRR array fabrication, electron beam lithography is not suitable in this case, since it leads to relatively long overall fabrication time. In contrast, complete structures, such as 16 μm × 16 μm SRR array (shown in Figure 21) can be fabricated via FIB writing within 20 minutes, which allows a large variety of different structures being fabricated and tested in a relatively short time.[66]

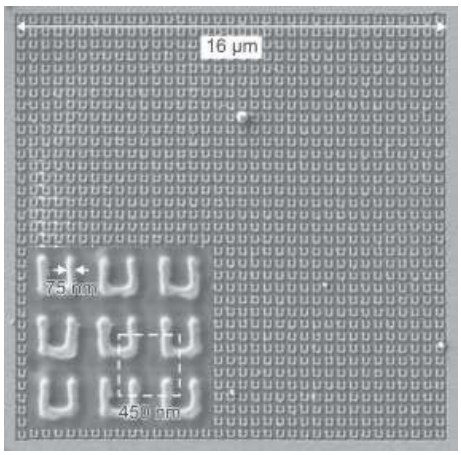

Figure 21: Electron microscope image of a 16 μm × 16 μm array of SRRs fabricated using FIB writing.[66]

A further advantage of FIB milling is the maskless direct writing with a large focus of depth, which enables the patterning of irregular and curved surfaces and nonplanar substrates that are difficult for resist spin coating. An et al. took this advantage of FIB milling and monolithically integrated light emitting diode (LED) device to AFM heads for scanning near-field microscopy. Due to surface tension effects and probe fragility, spin coating process is not well suitable for placing either e-beam resist or active organic layers onto a scanning probe cantilever. The active region on the cantilever was formed by milling the insulator with a focused gallium ion beam.[67]

Conventional processing methods such as photolithography, dry and wet etching can be used for 3D structure fabrication. However the parallel etching of the above mentioned methods can only be used to fabricate 3D structures with the same depth. In contrast, FIB milling allows varied milling depth over a pattern. Structures with curved surface and/or sloped sidewalls can be achieved by varying the ion dose pixel by pixel. In addition, the changeable ion beam incident angle and rotatable stage enable milling from different directions. Figure 22 shows an example of 3D nano-wine glass fabricated by using FIB system as a lathe. By rotating the stage similar to a precision motor driven system, the ion beam was operated as a nano-lathe to shape the axial symmetric structure. The schematic fabrication procedures are shown in Figure 23. Firstly a cylindrical column was made by removing unnecessary parts from the specimen attached to the rotating stage. The intermediate milling was carried out to make a dumbbell like rough shape of the glass from the cylinder. The final milling was carried out by making bit map expressing the glass outline.[68]

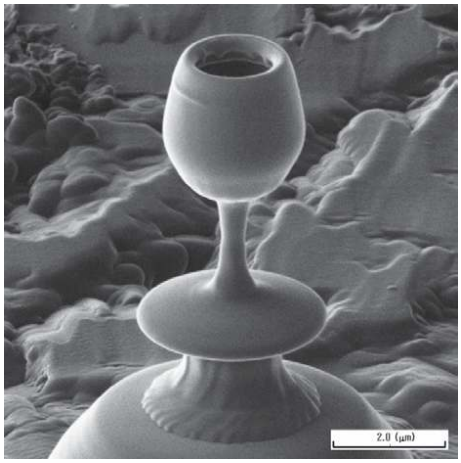

Figure 22: Scanning ion microscope image of nano-wine glass fabricated by FIB milling.[68]

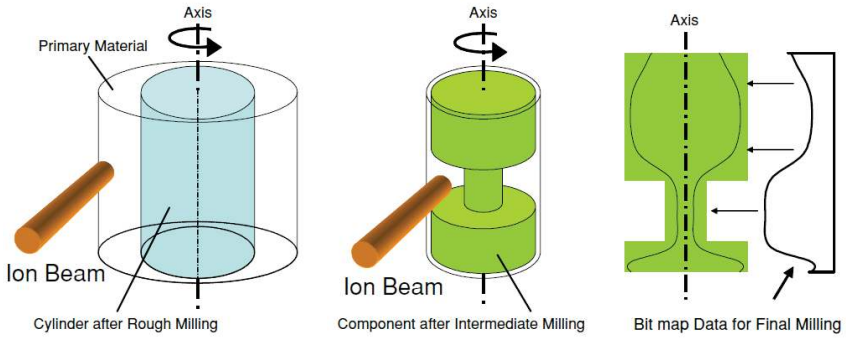

Figure 23: Schematic process flow of forming the wine glass outline with the nano-lathe: (a) rough milling; (b) intermediate milling; (c) final milling.[68]

2.6.3.2 FIB deposition Besides FIB milling, FIB deposition also plays a special roll in micro and nanofabrication. FIB deposition, also known as FIB CVD, enables the deposition of complex three dimensional shapes with overhanging features. The key to this technique is the possibility to deposit features that extend beyond the already present or previously deposited structure underneath, in which way an overhang can be created. As the deposition proceeds layer by layer, in each layer the new material extends a bit more over the previously deposited layer. Various 3D structures have been fabricated utilizing this technique. An example is the fabrication of various shapes of 3D nano-rotors with diamond like carbon structures using phenanthrene ($C_{14}H_{10}$) vapor precursor. The rotors were fabricated using 100 nm thick nano-sheet by shaping in the free space. Figure 24 shows a flat rotor (Figure 24a) fabricated on a silicon surface and two four wings rotors (Figure 24b and 24c). Rotors were rotated by either an electrostatic attractive force or by an aerodynamic force.[69]

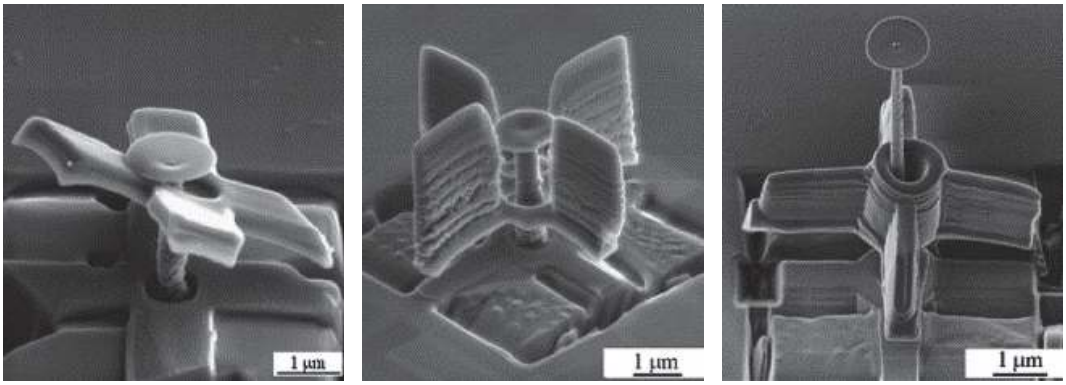

(a) (b) (c)

Figure 24: Nano-rotors fabricated by FIB deposition: (a) flat rotor with 5.5 μm diameter, 1.2 μm wing width and 0.57 μm wing thickness; (b) four wings rotor with 6 μm diameter, 3 μm wing height, 500 nm wing width and 2.6 μm axle length; (c) four wings rotor with 6 μm diameter, 2 μm wing height, 500 nm wing width and 6.4 μm axle length.[69]

2.6.3.3 Surface modification with FIB system In addition to the direct fabrication methods of milling and deposition, ion implantation by FIB can be used for material surface modification. One advantage of FIB implantation is the maskless patterning of line width as narrow as 10 nm. Furthermore, the dose can be varied pixel by pixel, which makes it possible for modification of devices and materials at length scales that are difficult to achieve using conventional processing techniques. Ion implantation and the associated secondary effects, such as interface mixing, have been used to fabricate quantum-effect structures including quantum wires, single-electron transistors, in-plane gated structures and diodes.[58]

It is well known that a high concentration p-type doping in silicon, such as boron doping, drastically reduces the silicon etch rate of the implanted region in alkaline etchants.[70] As a p-type dopant, gallium FIB implantation into silicon can serve as a masking method for silicon wet and dry etching. As the FIB ion energy is typically 10-50 keV, the resulting implanted layers are very shallow, usually under 50 nm. The critical dose for effective etch stop is around 1×10^{15} ions/cm^2, which may vary according to etch method specifics. The critical dose can be obtained within only a few seconds on small areas (for example 10 μm × 10 μm) using moderate beam currents (typically 100 pA). The amorphizaion dose of silicon is 1×10^{14} ions/cm^2, thus the implanted regions for masking are completely amorphous. Additionally, sputtering of the sample surface take place when the dose is above 1×10^{16} ions/cm^2. This effect can be exploited to realize three dimensional features.[58]

Combining the arbitrary patterning by FIB and anisotropic silicon etching in alkaline solutions, freestanding cantilevers and cones can be fabricated. Sievilä et al. fabricated ultra-narrow cantilevers and bridges on <110> silicon utilizing the thin insoluble amorphous Ga^+ doped silicon as masking layer (Figure25). By aligning the structure 45º off the <110> directed main axes on the substrate, the (100) planes appeared in parallel to the direction of the beams and formed 90º fast etching sidewalls, which led to the

structure release during TMAH etching.[71] By extending vertical FIB milling to several micrometers, devices with 30 nm thick vertical sidewalls can be fabricated. Nanocup fabricated by milling a 200 nm diameter and a few micrometer deep hole in silicon by FIB is shown in Figure 26. Subsequent KOH wet etching yielded nanocup with ultra-small volume around 3×10^{-8} nL.[72]

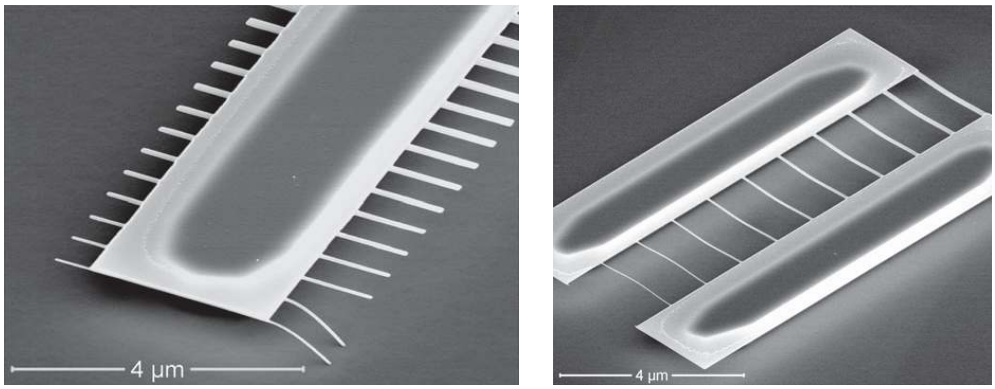

(a) (b)

Figure 25: (a) A series of freestanding cantilevers on <100> silicon substrate. The implantation dose was 4×10^{15} ions/cm^2. The lengths of the cantilevers are 0.5 µm (left) and 1 µm (right), the thickness is approximately 50 nm and the width of the narrowest beams is 35 nm. The stiction of two bridges on the substrate is derived from drying step after wet etching. (b) A series of 2 µm long freestanding bridges. The implantation dose was 2×10^{15} ions/cm^2. The widths range from 25 to 145 nm.[71]

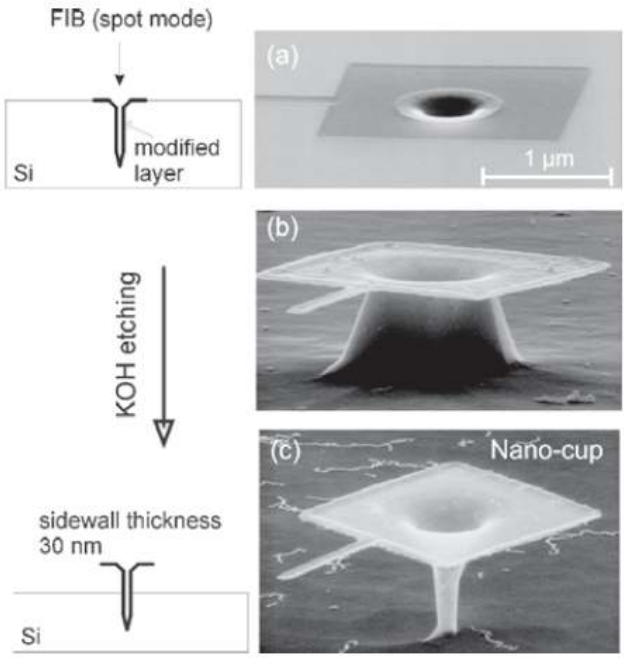

Figure 26: Process sequence for a nanocup: (a) after milling a 200 nm diameter hole in silicon; (b) after 10 minutes KOH etching; (c) after 15 minutes KOH etching.[72]

Gallium ion implanted silicon can also serve as etch mask for high aspect ratio nanostructures by cryogenic DRIE. Chekurov et al. investigated the possibilities of applying this method for high aspect ration 3D nanostructures fabrication by cryogenic plasma etching and promising results have been achieved.[73] The speed of FIB patterning was greatly enhanced since only a thin surface layer (around 30 nm) needed to be modified to form the etch stop mask. Etch selectivity between gallium doped and non-doped silicon was over 1000:1. The gallium ion dose effect on etch resistance of silicon in SF_6/O_2 plasma etching at cryogenic temperature was also studied. The threshold value of 2×10^{15} ions/cm^2 was found for any etch resistance to be observed, and 2×10^{16} ions/cm^2 was suggested to form masking layer with high selectivity. The dose dependent mask resistance can be applied to create 3D objects in a single etch step as shown in Figure 27a. They also demonstrated the most demanding application of this method to create low loading narrow nanopillars with high aspect ratio (Figure 27b). Later on Henry et al. determined the critical implanted gallium dose in silicon to achieve a desired etch depth for both Pseudo Bosch (SF_6/C_4F_8) and cryogenic fluorine (SF_6/O_2) silicon etching. Taking advantage of the undercut in DRIE for small dimension masking features, Henry et al. also fabricated suspended silicon nanowire by patterning a rectangle shape connecting two pillars followed by cryogenic DRIE.[74] Figure 28 shows the SEM image of institute logo of former Helsinki University of Technology fabricated by gallium FIB implantation in silicon substrate, followed by cryogenic DRIE.

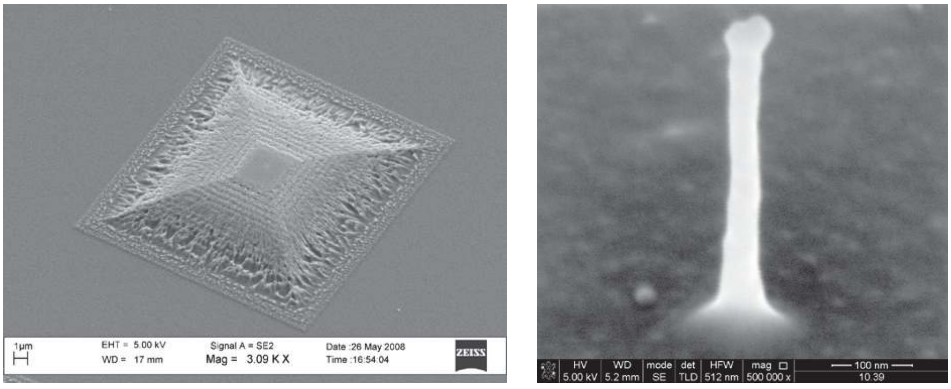

(a) (b)

Figure 27: (a) 3D structure created in a single 1 minute etch step by using 20 linearly increasing doses from 1.75×10^{14} ions/cm^2 (at rim) to 3.5×10^{15} ions/cm^2 (at central square area). The height of the resulting structure is 1.6 µm. (b) Single pillar with 40 nm diameter and 600 nm height.[73]

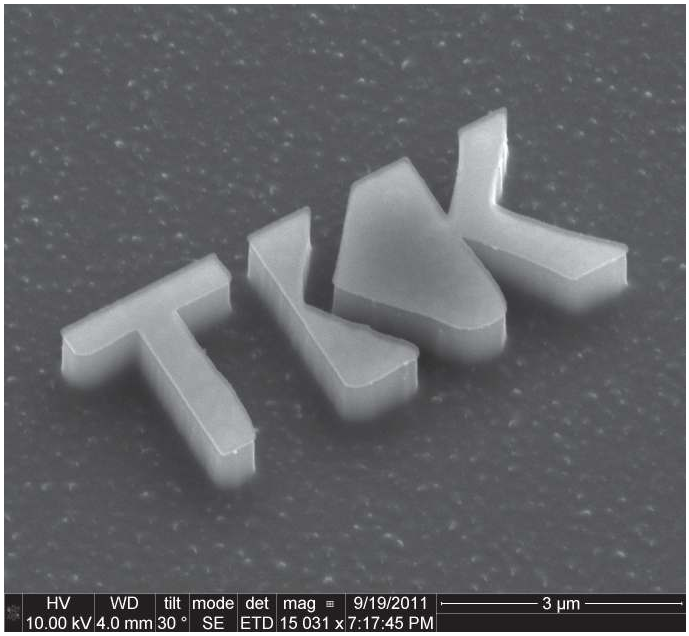

Figure 28: SEM image of institute logo of former Helsinki University of Technology fabricated by gallium FIB implantation followed by cryogenic DRIE of silicon (Courtesy Nikolai Chekurov).

3 Experimental section

3.1 Simulation of ion distribution

Sufficiently high ion implantation dose is required for the FIB patterning of an Al_2O_3 mask to give distinct chemical reactivities of the irradiated and non-irradiated areas. Meanwhile, gallium ion implanted silicon can also be used as an etch stop mask for fabrication of high aspect ratio silicon structures by DRIE. Thus during the gallium ion irradiation on the Al_2O_3 mask, ion penetration into silicon substrate should be avoided. In addition, wet etching of an excessively thick Al_2O_3 layer will aggravate the undercut problems. To gain a view of the penetration length and distribution of gallium ions in the Al_2O_3/Si stack, the FIB process was simulated with Stopping and Range of Ions in Matter (SRIM), which is an ion impact analysis software program utilizing Monte Carlo simulation.[59] The ion energy was set to be 30 keV in accordance with the experimental value. The thickness of silicon substrate was set to be 100 nm, and the program was run with the following thicknesses of Al_2O_3 on silicon: 30 nm, 40 nm and 50 nm.

3.2 Hard mask fabrication and silicon etching

3.2.1 Mask fabrication and silicon DRIE process overview

The patterning of Al_2O_3 hard mask for silicon DRIE is a two-step process including FIB irradiation and wet etching. The schematic process flow is depicted in Figure 29. Firstly the Al_2O_3 layer is deposited on silicon substrate by ALD (Figure 29a). Gallium ion FIB is then applied for maskless hard mask patterning. A simple ion implantation with proper dose is sufficient for pattern transfer to the Al_2O_3 mask without material removal in this step. The gallium FIB irradiation renders the etch selectivity between irradiated and non-irradiated parts for both Al_2O_3 and silicon substrate. Thus the physical patterns can be revealed by Al_2O_3 wet etching. However surface material removal may also take place, because high dose FIB results in sputtering of the specimen. The representative FIB patterning profiles are compared in Figure 29b. The bar pattern on the left is transferred by low dose ion implantation without evident surface damage. When the ion dose increases, Al_2O_3 milling takes place, leaving the milling frontier with gallium ion implantation as well (bar pattern in the middle). When the ion dose is extremely high, ion beam mills through the Al_2O_3 layer and continues into the silicon substrate, leaving the silicon milling frontier Ga^+ implanted (bar pattern on the right). The following wet etching releases the bar patterns on the Al_2O_3 hard mask (Figure 29c) and the sample is ready for silicon DRIE. In Figure 29d, it is clearly shown that over high irradiation doses lead to the failure of mask patterning due to the gallium invasion into silicon, which instead turns out to be the silicon etch stop mask in DRIE.

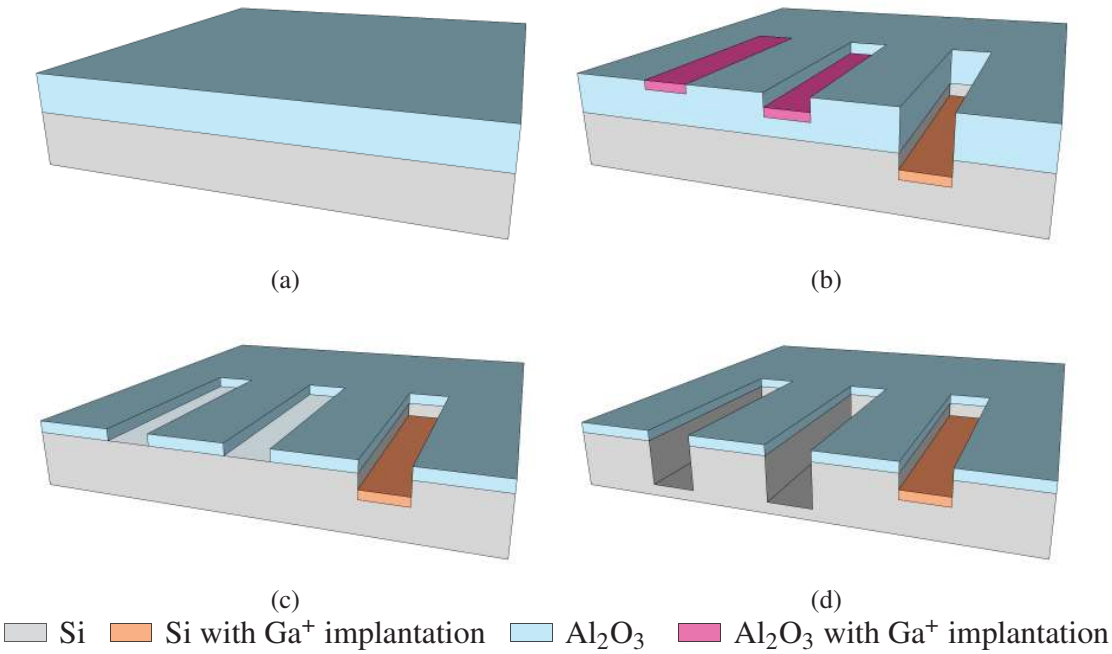

Figure 29: Schematic cross-section view of process flow for Al_2O_3 hard mask patterning and silicon DRIE: (a) Al_2O_3 ALD on silicon substrate; (b) FIB patterning of the Al_2O_3 mask; (c) Al_2O_3 mask wet etching in aluminum etchant; (d) silicon DRIE with Al_2O_3 mask. Ion implantation in lateral dimension, sidewall imperfection and surface damage are neglected in the drawing. Legend colors are taken from cross-section.

Sufficient thickness of the Al_2O_3 layer is required to protect the underlying silicon substrate from Ga^+ contamination. On the other hand, due to the isotropic nature of Al_2O_3 wet etching, thickness of the Al_2O_3 layer should also be minimized to reduce the undercut. The undercut development during the wet etching of Ga^+ FIB patterned Al_2O_3 layer is illustrated in Figure 30. In Figure 30a, the dashed lines from top to bottom represent the trend of etch frontier proceeding. In theory, the maximum mask dimension offset in one direction is equivalent to the removed thickness of the Al_2O_3 layer. The resulting mask profile is shown in Figure 30b, which clearly shows the increased width of the fabricated Al_2O_3 mask compared to the digital mask dimension.

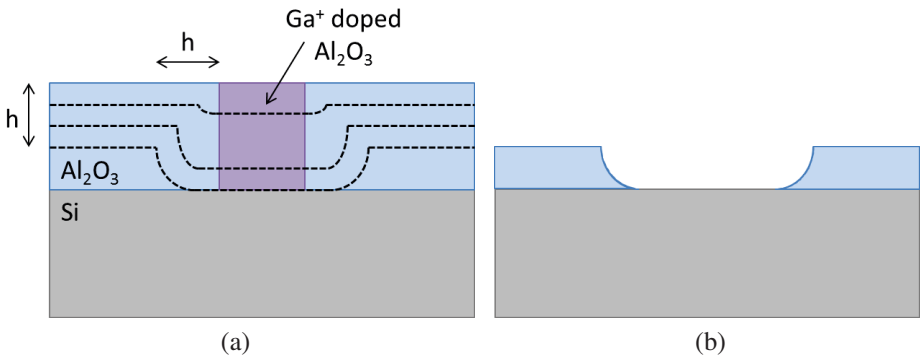

Figure 30: Schematic illustration of the undercut developed in the course of Al_2O_3 wet etching: (a) Ga^+ FIB irradiated Al_2O_3 layer on silicon substrate with estimated etch profile evolution; (b) Al_2O_3 mask profile after wet etching.

3.2.2 Al_2O_3 mask preparation

100 mm silicon wafers were used as substrates. Before the masking Al_2O_3 layer deposition, the wafers were sawed into 10 mm × 10 mm square shaped chips to carry out individual test. The chips were washed in acetone, isopropanol and distilled water (DIW) successively assisted with ultrasound. 50 nm and 100 nm Al_2O_3 films were grown by ALD in Thin Film Systems TFS-500 reactor (Beneq Oy, Finland), utilizing TMA as the metal precursor and H_2O as oxygen precursor. The process was conducted at 220 ºC and nitrogen was used as a carrier gas.

Before the Al_2O_3 mask patterning, etch rate of non-irradiated Al_2O_3 film in aluminum etchant (H_3PO_4:HNO_3:H_2O) was tested at the temperature of 50 ºC. Etch rates ware calculated by dividing the Al_2O_3 thickness difference before and after etching by the corresponding etch time. The etch tank was stirred before etching each chip to improve the temperature uniformity and composition homogeneity of the etchant solution, which maintains the consistence of etch condition for each test. Chips were rinsed with DIW immediately after etching and dried with nitrogen. This test gave the guideline to estimate the etch time to achieve certain mask thickness by time controlled etching. An etch rate of 9.2 nm/min was obtained as shown in Figure 31.

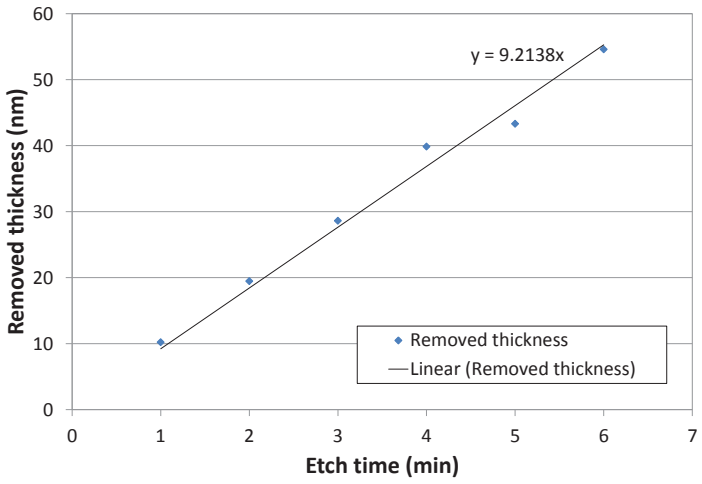

Figure 31: The removed thickness of Al_2O_3 at the corresponding etch time in aluminum etchant at 50 ℃.

Mask patterning was done by maskless FIB patterning followed by Al_2O_3 wet etching in aluminum etchant, taking advantage of the etch rate difference between FIB irradiated and non-irradiated Al_2O_3 in wet etchant. Helios Nanolab 600 dual beam system was used for local gallium FIB implantation. Serpentine scanning routine was applied for patterning all samples in this work. An extraction voltage of 30 kV was used for both mask parameters optimization test and resolution test. In the mask parameters optimization test, optimal gallium irradiation dose and wet etching time were first investigated. Patterning was done on silicon chips with 100 nm thick Al_2O_3 layer. Irradiation doses 2×10^{13} ions/cm^2, 2×10^{14} ions/cm^2, 2×10^{15} ions/cm^2, 2×10^{16} ions/cm^2, 2×10^{17} ions/cm^2 and 2×10^{18} ions/cm^2 were chosen to form the test pattern. Test pattern was designed to be parallel bars with different irradiation doses in order to give ease for structure depth characterization with AFM. Al_2O_3 was etched in aluminum etchant for different times from 0.5 to 5 minutes. Trench depth was then measured by AFM and the thickness of remained Al_2O_3 layer was measured by ellipsometer.

When the potential optimal gallium FIB doses and Al_2O_3 etch time were estimated from the dose test result, these values were used to carry out resolution test. Irradiation doses 6×10^{15} ions/cm^2, 8×10^{15} ions/cm^2 and 2×10^{16} ions/cm^2 were chosen to test the mask resolution for different features. Ion beam with FWHM diameter of 14 nm was used for resolution mask patterning. A digital resolution mask containing line, round via, square via and ring via features was used for Al_2O_3 etch mask patterning. The mask design in shown in Figure 32. The patterning was done on 50 nm thick Al_2O_3 mask and the wet etching time of the FIB patterned chip in aluminum etchant was 4 minutes.

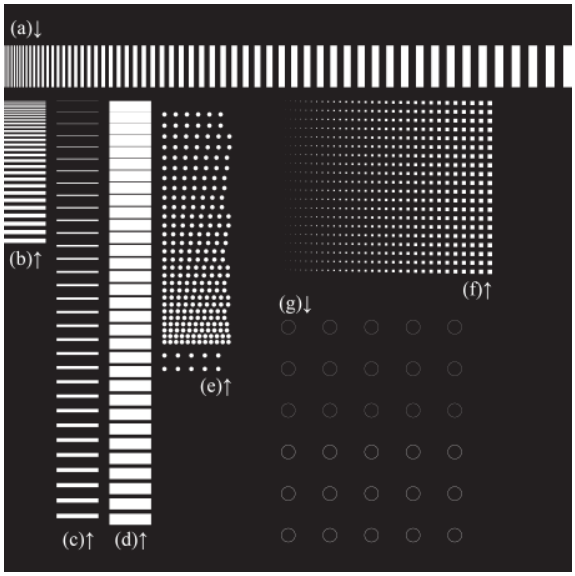

Figure 32: Digital resolution mask with (a) vertical line, (b), (c) and (d) horizontal line, (e) round via, (f) square via and (g) ring via features.

3.2.3 Inductively coupled plasma etching

Silicon chip with resolution mask was etched in an inductively coupled plasma reactive ion etcher (ICP-RIE) Oxford Instrument's PlasmaLab System 100. The process was conducted at -120 ºC and the etch time was 12 seconds. High density SF_6/O_2 plasma was generated by an inductively coupled plasma (ICP) source at 13.56 MHz and ion energies were controlled separately with a capacitively coupled plasma (CCP) operated at also 13.56 MHz. The SF_6/O_2 gas flow was 40/6.2 sccm. An ICP power of 800 W combined with a CCP (RIE) power of 3 W provided a strong chemical etching with minimal mask erosion. Etched structures were characterized with SEM in Helios Nanolab 600 dual beam system.

4 Results and discussion

4.1 Optimization of masking layer parameters

4.1.1 Testing dose selection

The developers of SRIM program Ziegler et al. have demonstrated that SRIM modeling for ion stopping calculation is in good agreement with experimental findings.[75] Thus it gives the guidance of mask parameter selection, such as ion dose, mask thickness and mask feature dimension compensation.

Figure 33 shows the SRIM modeling of Ga^+ ion distributions in Al_2O_3/Si stacks with the corresponding Al_2O_3 thickness (30 nm, 40 nm and 50 nm), when the ion energy is 30 keV. In all the distribution curves, Ga^+ ions are absent in the range of a couple nanometers under the Al_2O_3 surface. Ga^+ ions start to appear from 1.5 nm to 3 nm under the Al_2O_3 surface and the ion concentration increases as the penetration depth increases until a peak is reached. This peak indicates the high local ion concentration during ion implantation which is in the 10-20 nm range under the Al_2O_3 surface. Followed by the peak is the gradual drop of ion concentration to a low level. Ion distribution profile gives the guideline to predict the ion irradiation induced property change of involved materials. It can be seen that when the thicknesses of Al_2O_3 layer are 30 nm and 40 nm, ions penetrate through the Al_2O_3 layer and spread into the silicon substrate. Ion spreading depths in silicon from the Al_2O_3/Si interface are 18.1 nm and 3.2 nm for 30 nm and 40 nm thick Al_2O_3 masks, respectively. When the Al_2O_3 mask reaches 50 nm, Ga^+ ions stay in the Al_2O_3 layer without spreading into the silicon substrate.

Ga^+ doped Al_2O_3 possesses higher chemical reactivity than non-doped counterpart. In contrast, Ga^+ doping works as etch stop mask for silicon machining. For this reason ion invasion into silicon substrate should be prevented or at least in good control. The literature shows that 2×10^{15} ions/cm^2 is the threshold of Ga^+ implantation dose in silicon for pronounced etch stop, below which evident etch resistance is not observed.[73] The effective ion dose contributing to silicon etch stop, which passes through the Al_2O_3 layer and spreads into silicon, can be calculated from the ion distribution profiles in Figure 33. Setting the equivalent mask dose on silicon as 2×10^{15} ions/cm^2, ion percentage held in silicon substrate and initial Ga^+ dose irradiated from the Al_2O_3 layer with corresponding thickness are shown in Table 6. The calculation does not take into account the sputter yield. It can be seen that initial Ga^+ dose applied to 30 nm thick Al_2O_3 mask below 4.17×10^{17} ions/cm^2 does not cause silicon etch stop and can be considered safe dose for mask patterning. For 40 nm thick Al_2O_3, this value increases to 1×10^{20} ions/cm^2.

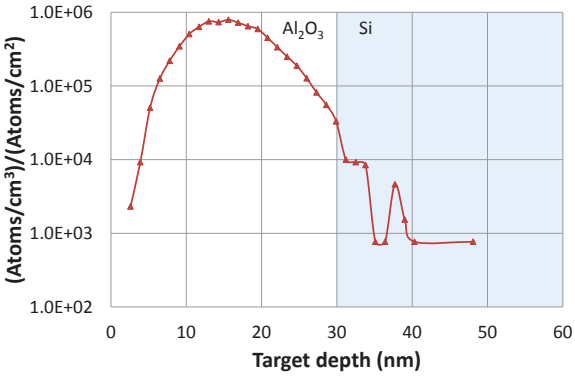

(a)

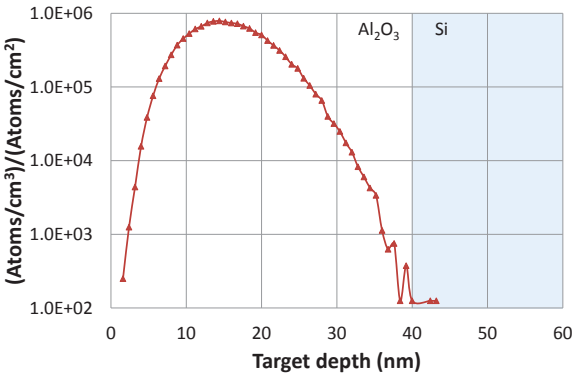

(b)

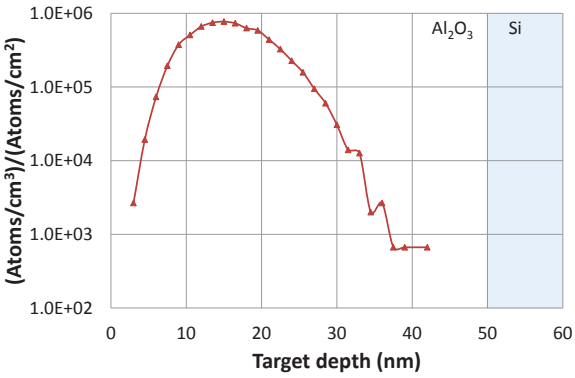

(c)

Figure 33: Ga^+ ion distributions in the Al_2O_3/Si stacks with the following Al_2O_3 thickness: (a) 30 nm; (b) 40 nm; (c) 50nm.

Al_2O_3 mask thickness (nm)	Dose percentage contributing to silicon etch stop	Initial Ga^+ dose to cause silicon etch stop through Al_2O_3 mask (ions/cm^2)
30	0.48%	4.17×10^{17}
40	0.002%	1×10^{20}

Table 6: Calculated ion percentage held in silicon substrate and equivalent initial gallium irradiation dose when silicon etch stop occurs. Sputter yield is not taken into account in the calculation.

Lateral Ga^+ ion distribution profile is also simulated with SRIM. Figure 34 shows the projected range and straggle of Ga^+ ion distribution in 50 nm thick Al_2O_3 layer. The incident angle is 0°, and the ion energy is 30 keV. As shown above in Figure 33c, the peak value of the gallium ion distribution in Al_2O_3 layer appears at the depth of 13.5 nm, and at this depth the lateral range is 3 nm with a standard deviation (straggle) of 4 nm.

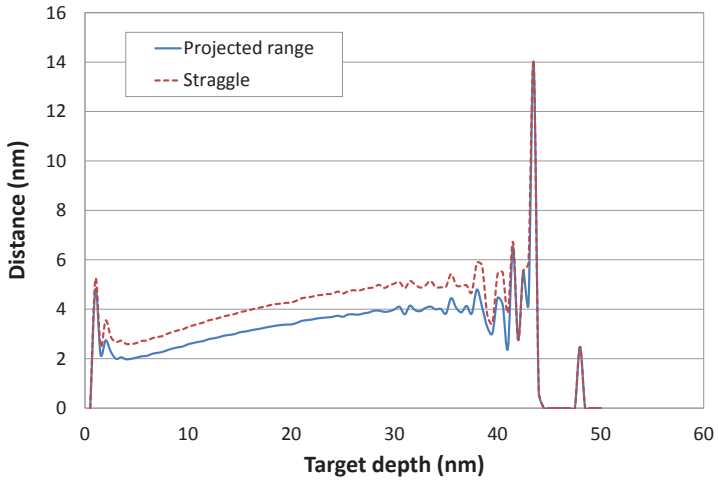

Figure 34: Projected range and straggle of Ga^+ ion distribution in 50 nm thick Al_2O_3 layer.

SRIM simulation is based on the assumption that the irradiated surface is planar and does not advance during the FIB process. As a result, the possible surface topography change can not be depicted graphically in SRIM simulation. However, highly non-planar surfaces usually occur during FIB process due to local material removal by ion beam milling, re-deposition, intermixing of different layer materials, etc. Accurate description of these phenomena should take into account both ion distribution and topographic development. In this work, the FIB milling depth is estimated from FIB milling rate of Al_2O_3, which was 0.095 μm^3/nC reported by Dai et al.[76] According to the calculation, the removed depth

is proportional to the ion dose, as shown in Figure 35. Ga^+ dose 6.6×10^{17} ions/cm^2 leads to complete removal of 100 nm thick Al_2O_3 layer. Lower doses 2×10^{16} ions/cm^2 and 2×10^{17} ions/cm^2 lead to 3 nm and 30 nm thick Al_2O_3 layers to be removed correspondingly.

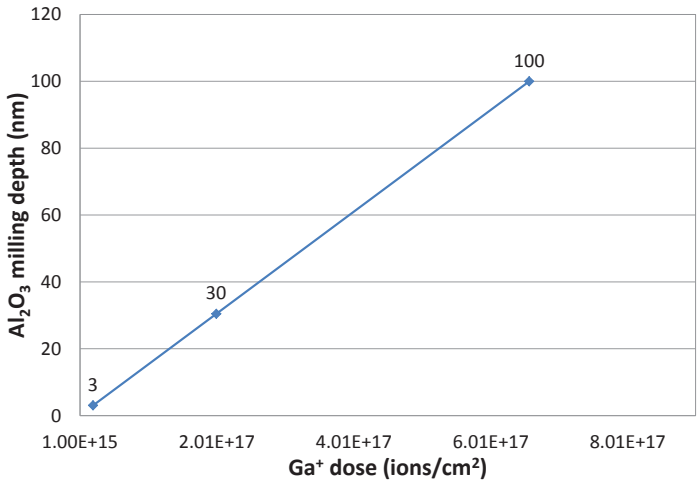

Figure 35: Ga^+ FIB milling depth of Al_2O_3 at the corresponding ion dose.

According to the safe dose calculation and milling depth estimation, the following Ga^+ doses were chosen for the dose optimization test: 2×10^{13} ions/cm^2, 2×10^{14} ions/cm^2, 2×10^{15} ions/cm^2, 2×10^{16} ions/cm^2, 2×10^{17} ions/cm^2 and 2×10^{18} ions/cm^2. The irradiation was done on 100 nm thick Al_2O_3 mask. Al_2O_3 mask thicker than 30 nm was chosen to find the ultimate mask thickness which can be achieved at each ion dose. Ga^+ irradiation is a known method for Al_2O_3 and silicon milling. Figure 36 shows the SEM images of gallium FIB irradiated Al_2O_3/Si stack patterned with parallel bar patterns. Bar shape patterns irradiated at 2×10^{14} ions/cm^2, 2×10^{15} ions/cm^2, 2×10^{16} ions/cm^2, 2×10^{17} ions/cm^2 and 2×10^{18} ions/cm^2 are visible under SEM and it is noticeable that some high doses resulted in removal of materials. 2×10^{18} ions/cm^2 Ga^+ FIB irradiation left deep trench on the stack, while doses 2×10^{17} ions/cm^2 and 2×10^{16} ions/cm^2 led to shallow damage in accordance with the mask pattern.

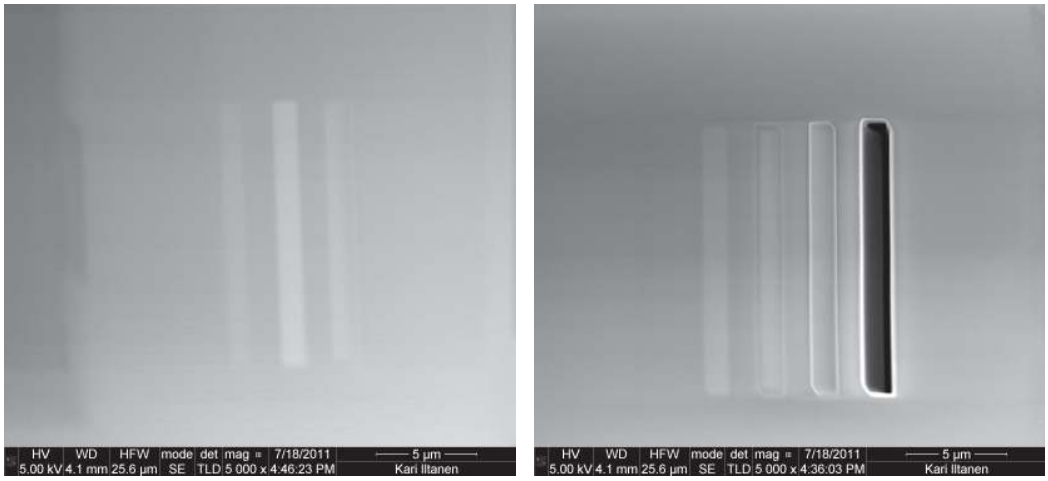

(a) (b)

Figure 36: SEM images of gallium FIB irradiated bar shape patterns on Al_2O_3/Si stack. Irradiation doses in each image from left to right are: (a) 2×10^{13} ions/cm^2 (pattern invisible), 2×10^{14} ions/cm^2, 2×10^{15} ions/cm^2 and 2×10^{16} ions/cm^2; (b) 2×10^{15} ions/cm^2, 2×10^{16} ions/cm^2, 2×10^{17} ions/cm^2 and 2×10^{18} ions/cm^2 (Courtesy Kari Iltanen).

AFM examination of the chip provides the topography profile of the structure, and the cross-section analysis reveals the milling depth during mask patterning. AFM images of the patterns irradiated with higher doses 2×10^{15} ions/cm^2, 2×10^{16} ions/cm^2, 2×10^{17} ions/cm^2 and 2×10^{18} ions/cm^2 are shown in Figure 37. In Figure 37a, damage done under doses 2×10^{15} ions/cm^2 and 2×10^{16} ions/cm^2 is not visible in the 2D top view of the Al_2O_3/Si stack. In the 3D portrait, areas patterned by gallium beam with the above mentioned two doses appear to be visible. However, trench depth irradiated by dose 2×10^{15} ions/cm^2 is not identified in the cross-section analysis of the AFM image, probably due to the surface roughness, possible noise during measurement and the equipment competence. 3 nm and 28 nm thick materials were milled away from the original surface when the irradiation doses were 2×10^{16} ions/cm^2 and 2×10^{17} ions/cm^2 respectively, which is in agreement with the estimated calculation to a good extend. 2×10^{18} ions/cm^2 Ga^+ ion irradiation milled through the 100 nm thick Al_2O_3 mask and continued 223 nm down to the silicon and resulted a total trench depth of 323 nm. Due to extensive damage to the substrate, irradiation dose 2×10^{18} ions/cm^2 is not applicable for the purpose of mask patterning in this work.

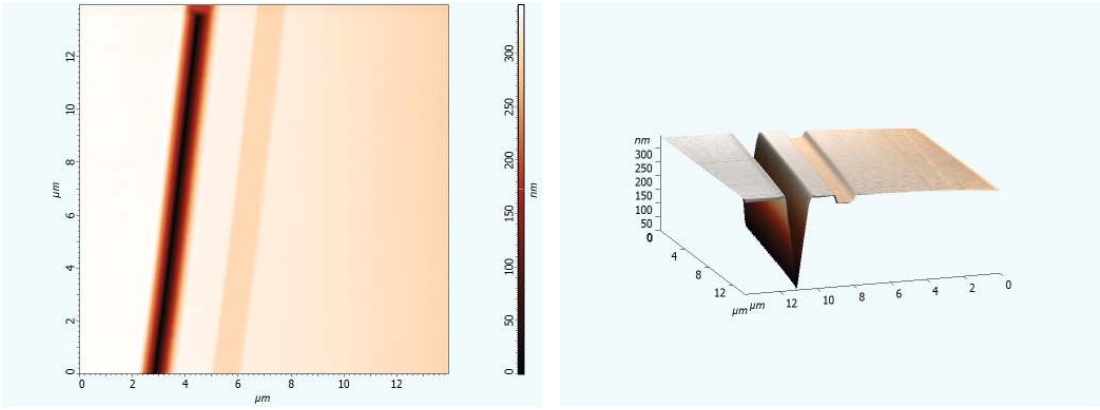

(a) (b)

Figure 37: AFM images of gallium FIB irradiated bar pattern on Al_2O_3/Si stack: (a) 2D portrait; (b) 3D portrait. In each image gallium FIB irradiation doses for trenches are 2×10^{18} ions/cm^2, 2×10^{17} ions/cm^2, 2×10^{16} ions/cm^2 and 2×10^{15} ions/cm^2 from left to right.

4.1.2 Wet etching of FIB patterned mask

Bar shape patterns on Al_2O_3 mask were released by wet etching in aluminum etchant after local gallium ion irradiation. Ion dose test establishes the basis of finding the optimal ion dose for various applications. Figure 38 shows the trench depth on the mask formed by different Ga^+ FIB doses and various wet etching times. The corresponding mask thickness of the non-irradiated area is also shown in the same figure. The average etch rate of Al_2O_3 acquired by linear fitting in this test is 7.3 nm/min, which is lower than the value acquired in the earlier Al_2O_3 etch rate test. This observation indicates that the etch rate of Al_2O_3 in aluminum etchant is strongly dependent on etch conditions such as temperature and the possible component change of the etchant. Except for the curve for dose 2×10^{17} ions/cm^2, other curves follow the same trend with two different regimes. At early times the trench depth keeps increasing, which will reach saturation after certain etch time. Higher gallium dose leads to evidently higher trench depth after 1 minute etching and on. The saturation time and the ultimate trench depth at the corresponding gallium ion dose are listed in Table 7. The saturation time of two lower doses is shorter than the other two of higher doses. The saturation time difference between doses 2×10^{13} ions/cm^2 and 2×10^{14} ions/cm^2 is not observed in this test, probably due to the time interval is not dense enough to detect the accurate transition point during the course of etching, and the same observation is found between doses 2×10^{15} ions/cm^2 and 2×10^{16} ions/cm^2. Upon the saturation time is reached, trench depth tends to remain stable and no longer depends on the etch time. Small fluctuation is observed for the ultimate trend depth, which is probably due to the measurement error resulted from the cross-section analysis of AFM images. Ultimate trend depth is equivalent to the upper limit of mask thickness at each irradiation dose.

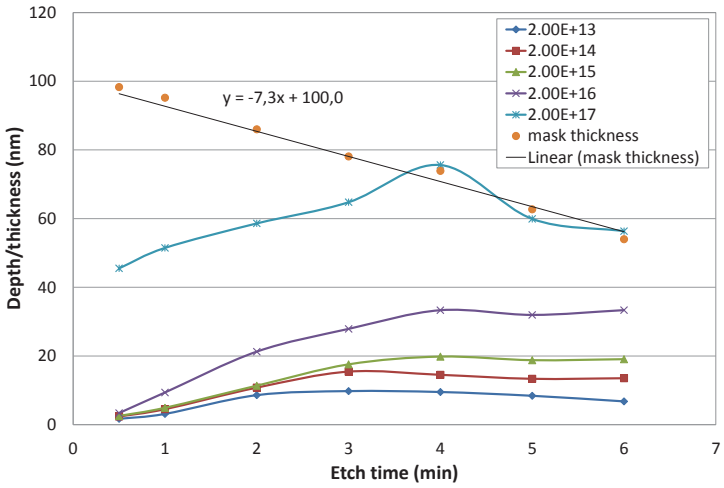

Figure 38: Trench depth on Al_2O_3 mask formed by various gallium doses and wet etch times and the corresponding mask thickness.

Ga^+ ion dose (ions/cm^2)	Saturation time (min)	Ultimate trench depth (nm)
2×10^{13}	3	8.2 ± 1.5
2×10^{14}	3	13.8 ± 0.7
2×10^{15}	4	19.2 ± 0.6
2×10^{16}	4	32.9 ± 0.9

Table 7: Saturation time and ultimate trench depth at corresponding gallium FIB dose.

The saturation time for ion dose 2×10^{17} ions/cm^2 is not acquired from this test, since the irradiated part on the Al_2O_3 mask has been removed completely before saturation is reached. The trench depth is apparently higher than that of the lower doses since beginning due to the high dose ion beam mills into the Al_2O_3 layer by irradiation. It keeps increasing at early times, which turns to be consistent with the mask thickness after 4 minutes. Mask thickness shrinkage is due to the constant wet etching of Al_2O_3 mask material. The small difference between the mask thickness and trench depth at later times is due to the error between the different characterization techniques, since neither gallium FIB irradiation nor aluminum etchant can attack the silicon substrate and the irradiated part stays clear once it is completely removed.

It is also noticeable from Figure 38 that in the cases without evident ion milling, the difference between trench structure development for different doses is not well pronounced after 0.5 minutes and it becomes evident during the etch process. This is also in agreement with the SRIM simulation results, that ion dose near the Al_2O_3 surface is relatively low and most ions accumulate in the range of 10 nm to 20 nm under the

surface. The slope of trench depth-time curve is an indication of the etch rate before saturation. A close inspection of the etch rate development is done by examining the average etch rate during certain time intervals as shown in Figure 39. Etch rate curve of dose 2×10^{17} ions/cm^2 distinguishes from others for a notable high etch rate at the beginning of the etch process, and then followed by a trend of declining. This is due to the high local ion density near surface, resulted from the removal of the originally near surface region of the Al_2O_3 layer with low ion density by FIB sputtering and the consequent ion precipitation during Al_2O_3 removal. According to the approximate calculation, when 28 nm thick surface milling takes place, ions can distribute as deep as 69 nm from the original Al_2O_3 layer surface.

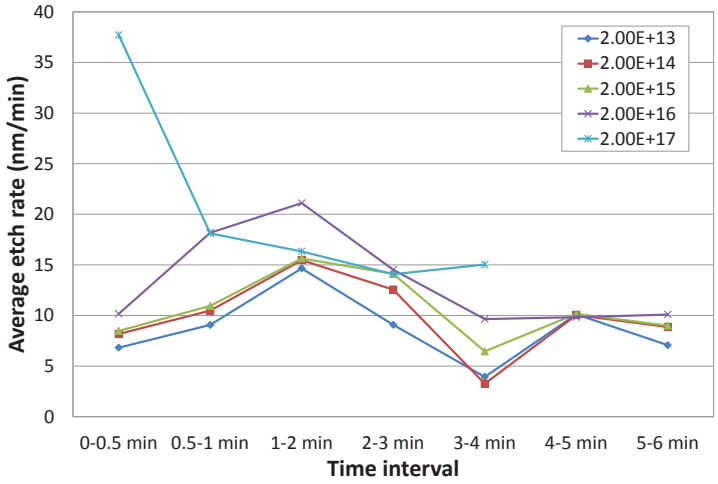

Figure 39: Average etch rate of gallium irradiated Al_2O_3 during indicated time intervals.

In Figure 39, etch rate curves of lower irradiation doses possess similar features that the average etch rate raises in early time intervals and drops to lower levels in later time intervals. Top average etch rate is observed in the time interval 1-2 minute for Al_2O_3 mask irradiated with gallium doses 2×10^{13} ions/cm^2, 2×10^{14} ions/cm^2, 2×10^{15} ions/cm^2 and 2×10^{16} ions/cm^2. It is notable that the average etch rates in the first and last examined intervals are similar with each other. This observation is consistent with SRIM modeling profile that the highest ion density region is in the neighborhood of 15 nm under the Al_2O_3 surface and the near surface and deeper than 30 nm regions have low ion densities. One abnormal observation in Figure 39 is that the average etch rates in the interval 3-4 minute drop to too low levels which are lower than that of non-irradiated Al_2O_3. This can be due to the measurement error and/or the variation of individual chip etching conditions, such as temperature, etchant composition and homogeneity, which influence the etch rate dramatically.

4.2 Al_2O_3 mask characterization

4.2.1 Selectivity

Numerical value of selectivity between silicon and Al_2O_3 mask is not acquired in this work since the measured thickness of Al_2O_3 mask was a couple of nanometers higher after DRIE than before etching. The measurement error can be due to the competence of ellipsometry, the moisture change in the Al_2O_3 mask and the development of native oxide at the Al_2O_3/Si interface. This observation is not contradictory to literature findings, which indicates a nearly infinite selectivity between silicon and Al_2O_3 mask in cryogenic DRIE of silicon. Selectivity of silicon to Al_2O_3 reached 700000 : 1 at cryogenic temperature reported by Grigoras et al.[23] According to this value, 2 µm thick silicon etching at cryogenic temperature leads to less than 0.1 nm thickness loss of the Al_2O_3 mask, which is hardly detectable by ellipsometry. Accurate selectivity can be measured by running the silicon cryogenic DRIE recipe to Al_2O_3 film for longer time and calculating the extremely low etch rate.

4.2.2 Resolution

According to the upper limit of mask thickness acquired at the corresponding Ga^+ irradiation dose from the dose test, irradiation doses 6×10^{15} ions/cm^2, 8×10^{15} ions/cm^2 and 2×10^{16} ions/cm^2 were chosen to test the mask resolution and to find out the optimal dose for masking. The starting Al_2O_3 film was 50 nm thick deposited by ALD and the wet etching time after gallium ion irradiation was 4 minutes. The FWHM diameter of FIB was 14 nm for resolution mask patterning.

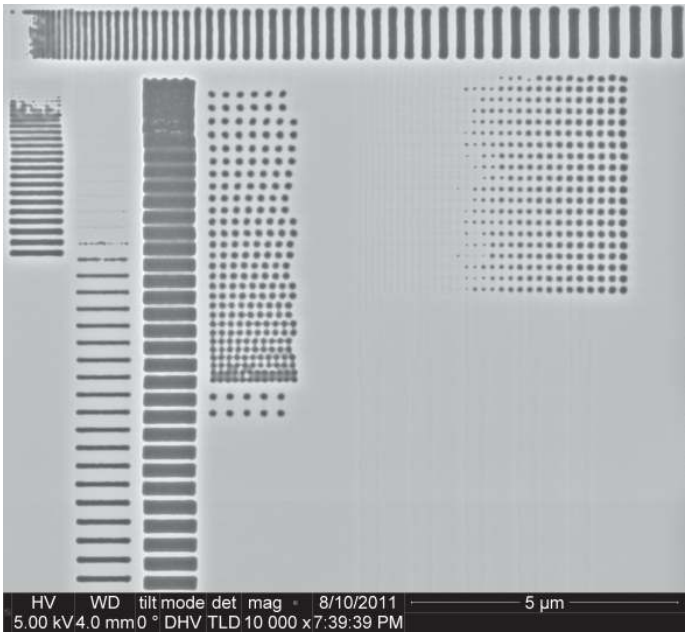

Figure 40: SEM image of top view Al_2O_3 mask with resolution test patterns fabricated by FIB irradiation with 8×10^{15} ions/cm^2 dose followed by wet etching.

Figure 40 gives a top view of the fabricated Al_2O_3 hard mask according to the digital mask shown in Figure 32, containing line, round via, square via and ring via features. It is clearly shown that line array patterns have better patternability and the feature sizes follow better regularity. On the contrary, mask quality for features with symmetrical geometry in both dimensions is obviously inferior. Severe distortion is observed for round via and square via features. Square vias are not completely opened until the edge width reaches 62 nm. Ring vias with annulus widths 3 nm and 6 nm failed to develop. A close view of the ion beam size, ion distribution range, undercut development and scan routine may give evidence of this observation.

As illustrated earlier in Figure 19, the ion intensity distribution of the FIB approximately resembles a Gaussian distribution. The intensity at the tail of the beam also contributes to FIB irradiation, with a dose lower than the beam center vicinity. Since the area covered by the tails is usually comparable with the central peak, it leads to the deviation of the ion distribution at the beam fringe and raises the inaccuracy for beam central region ion dose. As shown in Figure 41, the ion dose superposition of an FIB with 14 nm FWHM during patterning is higher for a 40 nm wide feature than that for a 10 nm wide feature. Taking into account the lateral ion straggle which is 4 nm at ion distribution peak depth, a single FIB scan with the FWHM diameter of 14 nm leads to an implantation region which is approximately 22 nm wide. The phenomenon that ions distribute away from the original incident points can be referred to as proximity effect. In this study, the proximity effect is mainly resulted from the Gaussian distribution of forward scattering ions. Besides, ion backward scattering, ion trajectory and atom recoiling also contribute to proximity phenomenon.

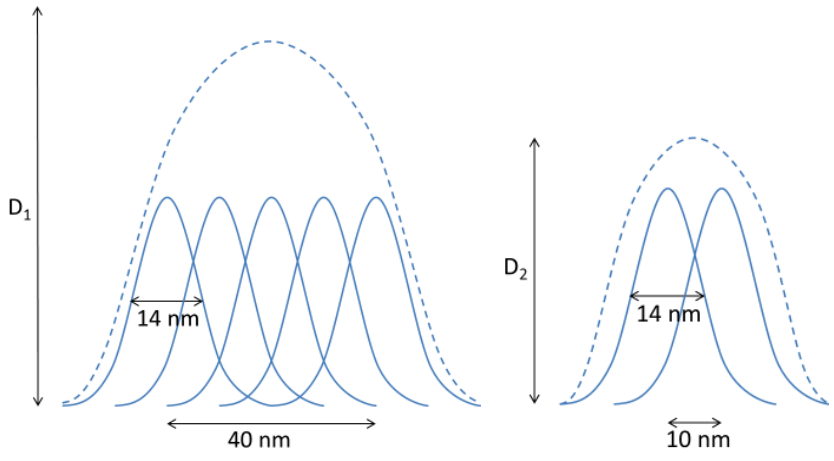

Figure 41: Schematic illustration of proximity effect for features with different dimensions (a) 40 nm and (b) 10 nm.

Due to proximity effect and ion density nonuniformity, feature size should reach a threshold value at least in one dimension to surpass the the ion injection deviation. An assumption of this value is one order higher than the ion lateral expansion, which is

80 nm. The deformation of round and square features is probably due to their all around similar dimension to the beam affected region, which is not large enough to prevail over the proximity effect. The failure of ring features is because of the small annulus widths, which are even smaller than the beam FWHM diameter.

The Al_2O_3 mask is released taking advantage of etch selectivity raised from ion implantation. Ideally, the mask lateral undercut at each side is equivalent to the removed Al_2O_3 thickness. In theory, for 4 minutes etching the maximum widening of the mask feature is $7.3nm/min \times 4min \times 2 = 58.4nm$. However, the nonuniform ion density distribution in both perpendicular and lateral dimensions may also affect the undercut development and generate Al_2O_3 mask sidewall roughness during wet etching. A rule of thumb for dimension compensation in mask designing can be estimated from statistical analysis of a certain amount of experimental results.

Scan routine may also affect the patterning accuracy of various features. Serpentine scan has been widely used in FIB systems, and spiral scan has been found giving advantage in FIB milling of curvy features. The routines of serpentine scan and spiral scan are compared in Figure 42. The serpentine scan routine applied in this work may also raise insufficiency for round feature patterning, which is similar to the observation in FIB milling.

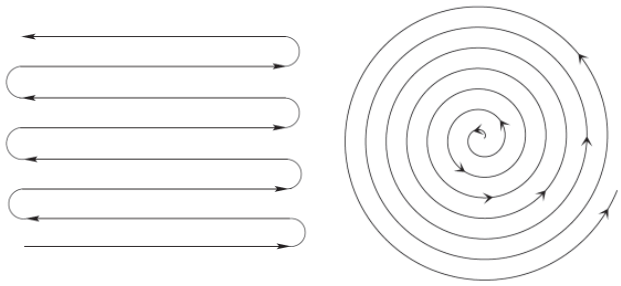

Figure 42: Schematics of (a) serpentine and (b) spiral scan routines. Regenerated from Reference [77].

Due to the inconsistent quality of round via, square via and ring via features on the achieved Al_2O_3 mask, the discussion of mask resolution is based on the vertical line array (a) and horizontal line array (d) shown in Figure 32. The vertical line array (a) contains equal width line and space pairs with linearly increasing width from left to right. The horizontal line array (d) contains lines with linearly increasing width from up to down and the spaces between the neighboring lines are identical.

Figure 43 shows the comparison between designed and actual masking Al_2O_3 line width in the vertical line array (a) for different irradiation doses. The linear trend of the mask dimension development as designed is observed for all doses. The missing points at each designed line width indicate the incompetence of the Al_2O_3 mask at the corresponding width. For each designed line width, the actual value of the Al_2O_3 mask increases as the

irradiation dose decreases. The difference of the feature size between the digital mask and fabricated Al_2O_3 mask is determined by the interplay between proximity effect, ion beam overlap, ion penetration depth distribution and contribution of the wet etching. The Al_2O_3 mask feature fabricated at dose 8×10^{15} ions/cm^2 is distinguished from others since the line widths possess the highest consistence with the designed values and the mask competence is of the widest range. Line widths of vertical lines irradiated at dose 6×10^{15} ions/cm^2 have positive deviation compared to designed widths in the whole range of the competent lines for masking, which indicates that at this dose, non-linear ion distribution through the Al_2O_3 surface overtakes the proximity effect, thus the final mask competent is lower than designed. On the contrary, when the irradiation dose reaches 2×10^{16} ions/cm^2, proximity effect dominates which leads to negative deviation of the vertical mask line width compared to designed value. Among the three tested doses, 8×10^{15} ions/cm^2 is the most preferable irradiation dose for mask competence resolution enhancement. It is noticeable that competent vertical line mask with the smallest width is acquired at the highest irradiation dose in this test. This reveals that proximity effect plays an important roll for Al_2O_3 mask patterning. Relatively high irradiation dose combined with proximity effect gives the possibility to fabricate small features approximate to 50 nm that can not be achieved with lower irradiation doses. Single line structure with small width on Al_2O_3 mask can be fabricated by taking into account the predictable deviation between designed and actual line width at certain irradiation dose.

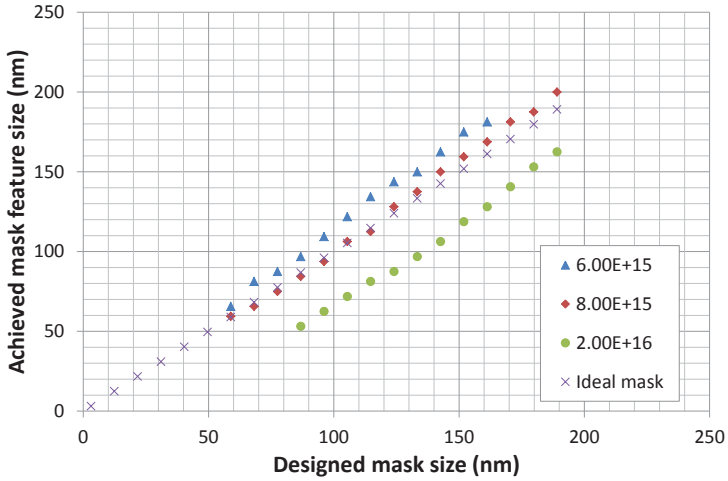

Figure 43: The comparison between designed and actual width of the Al_2O_3 masking lines in the vertical line array for the indicated doses.

The resolution of vertical lines on the mask is characterized by maximum amount of equal width line and space pair per 1 μm and average line/space width ratio. As shown in Figure 44, the maximum line and space pair numbers per 1 μm of vertical lines on Al_2O_3 mask fabricated with doses 6×10^{15} ions/cm^2 and 8×10^{15} ions/cm^2 reach the same value

7. When the irradiation dose increases to 2×10^{16} ions/cm^2, this value drops to 5 which is inferior to that of the Al_2O_3 mask fabricated with other two doses. The average line/space ratio decreases as the irradiation dose increases for mask fabrication. When the irradiation dose is 8×10^{15} ions/cm^2, the average line/space ration of vertical lines on Al_2O_3 mask is 0.95, which is to a big extend close to the designed value 1. This also gives evidence that the optimal dose for vertical line feature patterning in 50 nm Al_2O_3 mask fabrication is 8×10^{15} ions/cm^2.

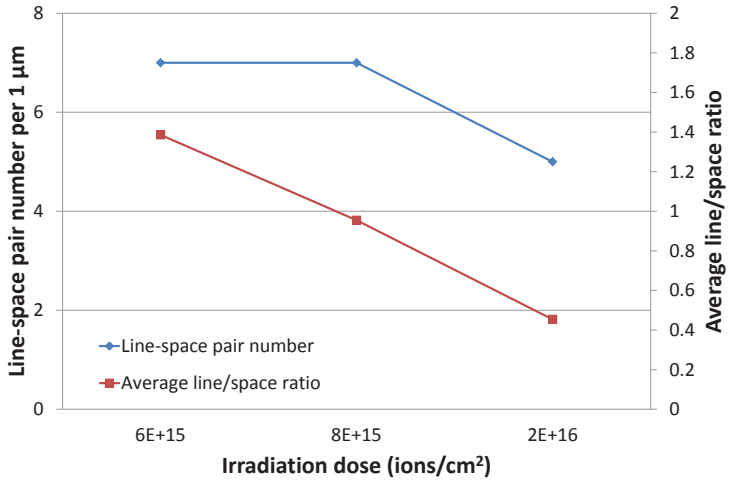

Figure 44: Maximum amount of equal width line and space pair per 1 µm and average line/space width ratio of the vertical line array for the indicated doses.

Figure 45 gives information of the deviation between designed and actual width of Al_2O_3 lines in the horizontal line array (d). Similarly to the observation from vertical line array, the actual width of horizontal line on the Al_2O_3 mask shows the trend to increase as the irradiation dose decreases. Differently, the deviation distribution is more complicated than that of the vertical line array. For the horizontal line array fabricated with all the tested doses, line width distribution shows inferior linearity compared to that of vertical line arrays. It is noticeable that for irradiation dose 6×10^{15} ions/cm^2 when the designed line width exceeds 80 nm, the achieved line width starts to keep constant in the tested range. The possible explanation is that when a threshold of designed line width is reached, proximity effect start to decay thus the actually achieved line width start to get close to the designed value. Similar behavior is also observed for dose 8×10^{15} ions/cm^2. Horizontal line widths fabricated with all the tested doses show considerable difference than designing, thus deviation correction should be taken into account in mask design for horizontal lines patterning. Different observations of mask quality for vertical and horizontal line arrays can be due to the vertical serpentine scan routine which benefits the former.

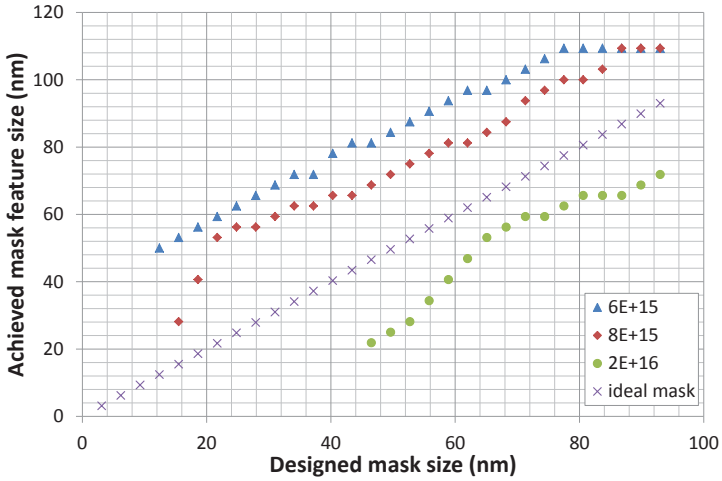

Figure 45: The comparison between designed and actual width of Al_2O_3 lines in the horizontal line array for the indicated doses.

The etch quality of the silicon substrate using the Al_2O_3 mask fabricated by FIB irradiation and wet etching after DRIE was examined with SEM. The silicon structure with horizontal line array patterns when FIB irradiation doses are 6×10^{15} ions/cm^2 and 8×10^{15} ions/cm^2 can be examined in Figure 46. Serious undercut is observed for small width lines. This insufficiency of silicon etching can be improved by optimizing DRIE parameters. For Al_2O_3 mask irradiated at both 6×10^{15} ions/cm^2 and 8×10^{15} ions/cm^2, undercut becomes less severe after the masking line width reaches 100 nm.

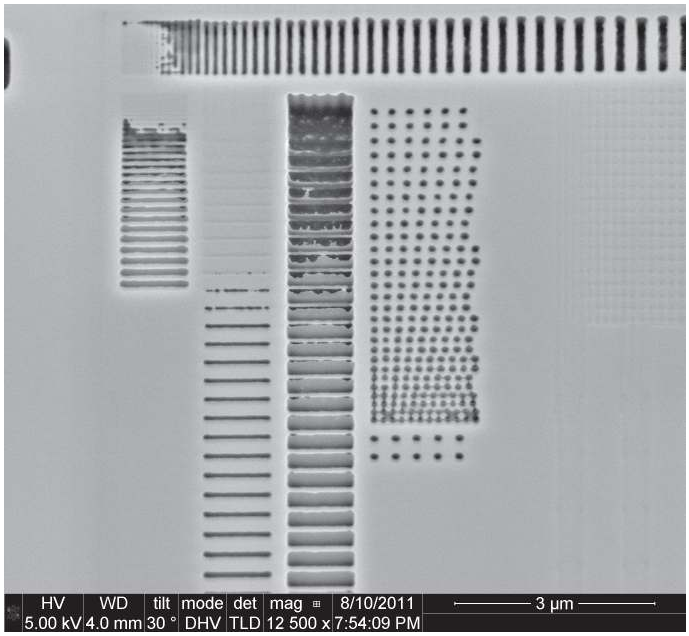

(a)

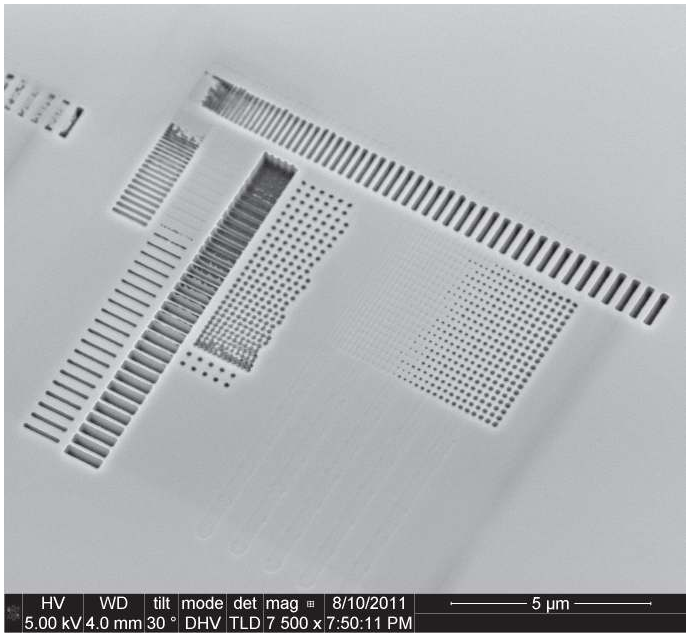

(b)

Figure 46: Cryogenic DIRE quality of the silicon substrate with resolution test Al_2O_3 mask fabricated by Ga^+ FIB irradiation with doses (a) 6×10^{15} ions/cm^2 and (b) 8×10^{15} ions/cm^2 followed by wet etching.

5 Conclusions and outlook

This work introduces a novel two-step process for Al_2O_3 hard mask patterning taking advantage of the increased etch rate of the gallium FIB irradiated Al_2O_3 compared to the non-irradiated counterpart in wet etchant. This method retains the universally recognized merit of FIB technique, which is digital controlled maskless patterning with high resolution, and provides additional flexibility of FIB application in micro- and nanofabrication. Gallium ion implantation renders enhanced chemical reactivity to Al_2O_3 which leads to the higher etch rate of Al_2O_3 in wet etchant. Aluminum etchant was chosen to be the etch solution in this work. The contrast on the Al_2O_3 layer developed from the etch rate difference can be readily utilized as hard mask for silicon DRIE once the irradiated area is completely removed. This method leaves out the photoresist applying and stripping processes compared to the conventional nano-patterning of Al_2O_3 hard mask with FIB or e-beam lithography and avoids resist related issues. It is also an alteration of p-type dopant FIB maskless patterning for silicon etch stop, which eliminates the undesirable lattice damage and contamination to silicon substrate in critical applications.

SRIM modeling shows that 50 nm thick Al_2O_3 layer is sufficient to prevent gallium ion penetration to the underlying silicon substrate when ion milling does not take place. To start patterning with thinner Al_2O_3 layer is also possible when the ion dose penetrating to the silicon substrate is insufficient to cause silicon etch stop. The highest achievable Al_2O_3 mask thickness is dependent on the wet etching selectivity between gallium FIB doped and the undoped Al_2O_3 which increases with the ion dose. FIB irradiation doses in the range of 2×10^{13}- 2×10^{16} ions/cm^2 were found to be applicable for Al_2O_3 mask patterning without evident surface damage. Ultimate selectivity induced Al_2O_3 mask thickness ranging from 8.2 nm to 32.9 nm can be acquired by applying ion doses between 2×10^{13} ions/cm^2 and 2×10^{16} ions/cm^2. Because a higher selectivity between gallium doped and undoped Al_2O_3 facilitates the pattern release during wet etching, FIB doses ranging from 6×10^{15} ions/cm^2 to 2×10^{16} ions/cm^2 are considered optimal irradiation doses for mask patterning. Taking into account the gallium spreading prevention in the substrate, 50 nm thick Al_2O_3 layer deposited on the silicon substrate is recommended to be the starting point. At 50 ºC, 4 minutes etching in aluminum etchant is found to be the optimal process to release pattern on a 50 nm thick Al_2O_3 layer irradiated with doses from 6×10^{15} ions/cm^2 to 2×10^{16} ions/cm^2.

Nearly infinite selectivity of silicon to ALD Al_2O_3 mask for silicon ICP-RIE is confirmed in this work, which is in accordance with literature findings. Among the tested doses, gallium FIB dose 8×10^{15} ions/cm^2 is distinguished for resolution enhancement. Masking capacity is evaluated as equal width vertical line and space pair mount per 1 μm, which is 7 pairs per 1 μm for best achieved result in this work. The serpentine scan routine utilized in this work favors line shape patterning parallel to the scan routine, and vector scanning is recommended for curvy nanostructure patterning.

It is noticed that the Al_2O_3 etch rate in aluminum etchant is unstable which raises difficulties for ultra-thin mask fabrication. Therefore, more reliable wet etchant selection can be an extension of this work to improve the process reproducibility. Due to the

solubility of Al_2O_3 in both acid and base, to find out the base etchant with precise etch control will broaden the compatibility of this method.

Resolution enhancement is consequentially the future trial emphasis based on current findings. The achievable mask capacity is affected by the interplay among proximity effect, ion beam overlap and undercut during mask etching. Cross section examination of the fabricated mask is anticipated to build on the correlation between lateral ion distribution and the sidewall profile, which can be used for mask sidewall condition optimization. Scan routine effect on mask resolution can also be tested, for example to apply spiral scan for round feature patterning.

This method is applicable for patterning of fragile substrate or substrate with fragile structures which do not stand spin coating and ultrasound processes. Besides, while Ga^+ FIB doping for silicon etch stop is suitable for bright field patterning, the two-step Al_2O_3 mask fabrication method provides the complementary approach for dark field patterning. This masking method is capable to produce arbitrary patterns and is suitable for trench array and via array fabrication. Trench and via array structures have a wide range of applications in microsystems technology, such as strainers for microfluidic devices and wave guide components for optoelectronic systems.

References

[1] G. E. Fuller, "Optical lithography," in *Handbook of Semiconductor Manufacturing Technology*, Y. Nishi and R. Doering, Eds. New York: Marcel Dekker, Inc., 2000, pp. 461–498.

[2] S. Franssila, *Introduction to Microfabrication*, 1st ed. Chichester: John Wiley & Sons Ltd, 2004.

[3] R. Pease and S. Chou, "Lithography and other patterning techniques for future electronics," *Proceedings of the IEEE*, vol. 96, no. 2, pp. 248–270, 2008.

[4] S. Franssila, *Introduction to Microfabrication*, 2nd ed. Chichester: John Wiley & Sons Ltd, 2010.

[5] R. Ito and S. Okazaki, "Pushing the limits of lithography," *Nature*, vol. 406, no. 6799, pp. 1027–1031, 2000.

[6] M. Totzeck, W. Ulrich, A. Göhnermeier, and W. Kaiser, "Semiconductor fabrication: Pushing deep ultraviolet lithography to its limits," *nature photonics*, vol. 1, no. 11, pp. 629–631, 2007.

[7] J. P. Silverman, "X-ray lithography," in *Handbook of Semiconductor Manufacturing Technology*, R. Nishi, Y; Doering, Ed. New York: Marcel Dekker, Inc., 2000, pp. 543–570.

[8] S. Chou, P. Krauss, and P. Renstrom, "Nanoimprint lithography," *Journal of Vacuum Science & Technology B: Microelectronics and Nanometer Structures*, vol. 14, no. 6, pp. 4129–4133, 1996.

[9] B. Tan, "Deep micro hole drilling in a silicon substrate using multi-bursts of nanosecond UV laser pulses," *Journal of Micromechanics and Microengineering*, vol. 16, p. 109, 2006.

[10] P. Wagler, U. Tangen, T. Maeke, H. Mathis, and J. McCaskill, "Microfabrication of a biomodule composed of microfluidics and digitally controlled microelectrodes for processing biomolecules," *Smart materials and structures*, vol. 12, p. 757, 2003.

[11] K. Addae-Mensah, S. Retterer, S. Opalenik, D. Thomas, N. Lavrik, and J. Wikswo, "Cryogenic etching of silicon: An alternative method for fabrication of vertical microcantilever master molds," *Microelectromechanical Systems, Journal of*, vol. 19, no. 1, pp. 64–74, 2010.

[12] K. Schade, *Mikroelektroniktechnologie (Microelectronics Technology in German)*. Berlin: Verlag Technik, 1991.

[13] K. Bean, "Anisotropic etching of silicon," *Electron Devices, IEEE Transactions on*, vol. 25, no. 10, pp. 1185–1193, 1978.

[14] B. Tang, K. Sato, and M. Gosálvez, "Sharp silicon tips with different aspect ratios in wet etching/DRIE and surfactant-modified TMAH etching," *Sensors and Actuators A: Physical*, in press, 2012.

[15] R. Zhou, H. Zhang, Y. Hao, and Y. Wang, "Simulation of the Bosch process with a string–cell hybrid method," *Journal of Micromechanics and Microengineering*, vol. 14, p. 851, 2004.

[16] G. Sun, X. Zhao, H. Zhang, L. Wang, and G. Lu, "3-D simulation of bosch process with voxel-based method," in *Nano/Micro Engineered and Molecular Systems, 2007. NEMS'07. 2nd IEEE International Conference on*. IEEE, 2007, pp. 45–49.

[17] F. Laermer, S. Franssila, L. Sainiemi, and K. Kolari, "Deep reactive ion etching," in *Handbook of silicon based MEMS materials and technologies*, V. Lindroos, M. Tilli, A. Lehto, and T. Motooka, Eds. William Andrew, 2009, pp. 349–374.

[18] B. Matthews and J. Judy, "Design and fabrication of a micromachined planar patch-clamp substrate with integrated microfluidics for single-cell measurements," *Microelectromechanical Systems, Journal of*, vol. 15, no. 1, pp. 214–222, 2006.

[19] M. Lee and M. Wu, "Thermal annealing in hydrogen for 3-D profile transformation on silicon-on-insulator and sidewall roughness reduction," *Microelectromechanical Systems, Journal of*, vol. 15, no. 2, pp. 338–343, 2006.

[20] T. Defforge, X. Song, G. Gautier, T. Tillocher, R. Dussart, S. Kouassi, and F. Tran-Van, "Scalloping removal on drie via using low concentrated alkaline solutions at low temperature," *Sensors and Actuators A: Physical*, pp. 114–120, 2011.

[21] I. Saraf, M. Goeckner, B. Goodlin, K. Kirmse, and L. Overzet, "Mask undercut in deep silicon etch," *Applied Physics Letters*, vol. 98, p. 161502, 2011.

[22] W. Wang, J. Ho, and P. Reinhall, "Deep reactive ion etching of silicon using an aluminum etching mask," in *Advanced Semiconductor Devices and Microsystems, 2002. The Fourth International Conference on*. IEEE, 2002, pp. 31–34.

[23] K. Grigoras, L. Sainiemi, J. Tiilikainen, A. Säynätjoki, V. Airaksinen, and S. Franssila, "Application of ultra-thin aluminum oxide etch mask made by atomic layer deposition technique," in *Journal of Physics: Conference Series*, vol. 61. IOP Publishing, 2007, p. 369.

[24] S. Tegen and P. Moll, "Etch characteristics of AlO in ICP and MERIE plasma etchers," *Journal of the Electrochemical Society*, vol. 152, p. G271, 2005.

[25] R. Ross and M. T. Pham, "Modification of the chemical properties of silicon by ion implantation with high doses of Ar and P," *Journal of Radioanalytical and Nuclear Chemistry*, vol. 50, no. 1, pp. 45–52, 1979.

[26] C. McHargue, J. Hunn, D. Joslin, E. Alves, M. Da Silva, and J. Soares, "Etching of amorphous Al_2O_3 produced by ion implantation," *Nuclear Instruments and Methods in Physics Research Section B: Beam Interactions with Materials and Atoms*, vol. 127, pp. 596–598, 1997.

[27] J. Bigarre, S. Fayeulle, D. Treheux, and N. Moncoffre, "Structural modifications of alumina implanted with zirconium, copper, and titanium ions," *Journal of applied physics*, vol. 82, p. 3740, 1997.

[28] P. Burnett and T. Page, "Criteria for mechanical property modifications of ceramic surfaces by ion implantation," *Radiation effects*, vol. 97, no. 3-4, pp. 283–296, 1986.

[29] C. McHargue, R. Kossowsky, and W. Hofer, *Structure-property relationships in surface-modified ceramics*. Kluwer Academic Pub, 1989.

[30] C. J. McHargue, P. S. Sklad, and C. W. White, "The structure of ion implanted ceramics," *Nuclear Instruments and Methods in Physics Research Section B: Beam Interactions with Materials and Atoms*, vol. 46, no. 1-4, pp. 79–88, 1990.

[31] C. W. White, C. J. McHargue, P. S. Sklad, L. A. Boatner, and G. C. Farlow, "Ion implantation and annealing of crystalline oxides," *Materials science reports*, vol. 4, no. 2, pp. 41–146, 1989.

[32] N. Moncoffre, "A comparison between ion implantation into sapphire and polycrystalline alumina," *Nuclear Instruments and Methods in Physics Research Section B: Beam Interactions with Materials and Atoms*, vol. 59, pp. 1129–1141, 1991.

[33] S. J. Zinkle, "Microstructure of ion irradiated ceramic insulators," *Nuclear Instruments and Methods in Physics Research Section B: Beam Interactions with Materials and Atoms*, vol. 91, no. 1-4, pp. 234–246, 1994.

[34] T. Hioki, A. Itoh, M. Ohkubo, S. Noda, H. Doi, J. Kawamoto, and O. Kamigaito, "Mechanical property changes in sapphire by nickel ion implantation and their dependence on implantation temperature," *Journal of materials science*, vol. 21, no. 4, pp. 1321–1328, 1986.

[35] M. Ritala and M. Leskelä, "Atomic layer deposition," in *Handbook of Thin Film Materials*, H. S. Nalwa, Ed. Academic Press, 2002, pp. 103–159.

[36] H. Kim, H. Lee, and W. Maeng, "Applications of atomic layer deposition to nanofabrication and emerging nanodevices," *Thin Solid Films*, vol. 517, no. 8, pp. 2563–2580, 2009.

[37] R. Puurunen, "Surface chemistry of atomic layer deposition: A case study for the trimethylaluminum/water process," *Journal of applied physics*, vol. 97, p. 121301, 2005.

[38] S. M. George, “Atomic layer deposition: an overview.” *Chemical reviews*, vol. 110, no. 1, pp. 111–113, 2010.

[39] E. Soininen, G. Härkönen, and K. Vasama, “3rd international conference on the science and technology of display phosphors,” *Huntington Beach, CA, USA*, p. 105, 1997.

[40] R. O. Törnqvist, J. Antson, J. Skarp, and V. P. Tanninen, “How the ZnS:Mn layer thickness contributes to the performance of AC thin-film EL devices grown by atomic layer epitaxy (ALE),” *Electron Devices, IEEE Transactions on*, vol. 30, no. 5, pp. 468–471, 1983.

[41] D. Theis, H. Oppolzer, G. Ebbinghaus, and S. Schild, “Cross-sectional transmission electron microscopy of electroluminescent thin films fabricated by various deposition methods,” *Journal of crystal growth*, vol. 63, no. 1, pp. 47–57, 1983.

[42] M. Leskelä and M. Ritala, “Atomic layer deposition chemistry: Recent developments and future challenges,” *Angewandte Chemie International Edition*, vol. 42, no. 45, pp. 5548–5554, 2003.

[43] V. Lujala, J. Skarp, M. Tammenmaa, and T. Suntola, “Atomic layer epitaxy growth of doped zinc oxide thin films from organometals,” *Applied surface science*, vol. 82, pp. 34–40, 1994.

[44] T. Dhakal, A. Nandur, R. Christian, P. Vasekar, S. Desu, C. Westgate, D. I. Koukis, D. J. Arenas, and D. B. Tanner, “Transmittance from visible to mid infra-red in AZO films grown by atomic layer deposition system,” *Solar Energy*, in press, 2012.

[45] M. D. Benoy, E. M. Mohammed, M. Suresh Babu, P. J. Binu, and B. Pradeep, “Thickness dependence of the properties of indium tin oxide (ITO) films prepared by activated reactive evaporation,” *Brazilian Journal of Physics*, vol. 39, no. 4, pp. 629–632, 2009.

[46] S. H. Jeong, J. W. Lee, S. B. Lee, and J. H. Boo, “Deposition of aluminum-doped zinc oxide films by RF magnetron sputtering and study of their structural, electrical and optical properties,” *Thin Solid Films*, vol. 435, no. 1, pp. 78–82, 2003.

[47] M. Kon, P. Song, Y. Shigesato, P. Frach, A. Mizukami, and K. Suzuki, “Al-doped ZnO films deposited by reactive magnetron sputtering in mid-frequency mode with dual cathodes,” *Japanese journal of applied physics*, vol. 41, no. 2A, pp. 814–819, 2002.

[48] H. Antson, M. Grasserbauer, M. Hamilo, L. Hiltunen, T. Koskinen, M. Leskelä, L. Niinistö, G. Stingeder, and M. Tammenmaa, “Characterization of thin-film electroluminescent structures by SIMS and other analytical techniques,” *Fresenius’ Journal of Analytical Chemistry*, vol. 322, no. 2, pp. 175–180, 1985.

[49] “International technology roadmap for semiconductors (ITRS), 2011 edition,” Semiconductor Industry Association, Tech. Rep., 2011.

[50] A. Lintanf-Salaün, A. Mantoux, E. Djurado, and E. Blanquet, "Atomic layer deposition of tantalum oxide thin films for their use as diffusion barriers in microelectronic devices," *Microelectronic Engineering*, vol. 87, no. 3, pp. 373–378, 2010.

[51] J. S. Williams, "Ion implantation of semiconductors," *Materials Science and Engineering: A*, vol. 253, no. 1, pp. 8–15, 1998.

[52] J. Lindhard and A. Winther, "Stopping power of electron gas and equipartition rule," *Matematisk Fysiske Meddelelser, Kongelige Danske Videnskabernes Selskab (Royal Danish Academy of Sciences and Letters)*, vol. 34, no. 4, 1964.

[53] P. M. Echenique, R. M. Nieminen, and R. H. Ritchie, "Density functional calculation of stopping power of an electron gas for slow ions," *Solid State Communications*, vol. 37, no. 10, pp. 779–781, 1981.

[54] R. B. Simonto, V. Class, Y. Erokhin, M. Mack, and L. Rubin, "Ion implantation," in *Handbook of Semiconductor Manufacturing Technology*, Y. Nishi and R. Doering, Eds. New York: Marcel Dekker, Inc., 2000.

[55] J. Lindhard, M. Scharff, and H. Schioett, "Range concepts and heavy ion ranges (notes on atomic collisions, II)," *Matematisk Fysiske Meddelelser, Kongelige Danske Videnskabernes Selskab (Royal Danish Academy of Sciences and Letters)*, vol. 33, no. 14, 1963.

[56] G. Gerlan and W. Dötzel, *Introduction to Microsystem Technology: A Guide for Students*. Chichester: John Wiley & Sons Ltd, 2008.

[57] R. M. Langford, "Focused ion beam systems: Application to micro- and nanofabrication," in *Encyclopedia of Materials: Science and Technology*, K. H. J. Buschow, R. W. Cahn, M. C. Flemings, B. Ilschner, E. J. Kramer, S. Mahajan, and P. Veyssière, Eds. Elsevier Ltd, 2010, pp. 1–13.

[58] S. Reyntjens and R. Puers, "A review of focused ion beam applications in microsystem technology," *Journal of Micromechanics and Microengineering*, vol. 11, pp. 287–300, 2001.

[59] J. Ziegler, J. P. Biersack, and U. Littmark, *The stopping and range of ions in solids*. New York: Pergamon Press, 1985.

[60] C.-S. Kim, S.-H. Ahn, and D.-Y. Jang, "Review: Developments in micro/nanoscale fabrication by focused ion beams," *Vacuum*, vol. 86, no. 8, pp. 1014–1035, 2012.

[61] M. T. Abramo and L. L. Hahn, "The application of advanced techniques for complex focused-ion-beam device modification," *Microelectronics and reliability*, vol. 36, no. 11-12, pp. 1775–1778, 1996.

[62] G. J. Athas, K. E. Noll, R. Mello, R. Hill, D. E. Yansen, F. F. Wenners, J. P. Nadeau, T. Ngo, and M. Siebers, "Focused ion beam system for automated MEMS prototyping and processing," vol. 3223, pp. 198–207, 1997.

[63] D. Freeman, S. Madden, and B. Luther-Davies, "Fabrication of planar photonic crystals in a chalcogenide glass using a focused ion beam," *Optics Express*, vol. 13, no. 8, pp. 3079–3086, 2005.

[64] F. Lacour, N. Courjal, M. Bernal, A. Sabac, C. Bainier, and M. Spajer, "Nanostructuring lithium niobate substrates by focused ion beam milling," *Optical materials*, vol. 27, no. 8, pp. 1421–1425, 2005.

[65] R. Langford, P. Nellen, J. Gierak, and Y. Fu, "Focused ion beam micro-and nanoengineering," *MRS Bulletin*, vol. 32, no. 5, pp. 417–423, 2007.

[66] C. Enkrich, F. Pérez-Willard, D. Gerthsen, J. Zhou, T. Koschny, C. Soukoulis, M. Wegener, and S. Linden, "Focused-ion-beam nanofabrication of near-infrared magnetic metamaterials," *Advanced Materials*, vol. 17, no. 21, pp. 2547–2549, 2005.

[67] K. H. An, B. O'Connor, K. Pipe, Y. Zhao, and M. Shtein, "Organic light-emitting device on a scanning probe cantilever," *Applied physics letters*, vol. 89, p. 111117, 2006.

[68] T. Fujii, K. Iwasaki, M. Munekane, T. Takeuchi, M. Hasuda, T. Asahata, M. Kiyohara, T. Kogure, Y. Kijima, and T. Kaito, "A nanofactory by focused ion beam," *Journal of Micromechanics and Microengineering*, vol. 15, pp. S286–S291, 2005.

[69] J. Igaki, R. Kometani, K. Nakamatsu, K. Kanda, Y. Haruyama, Y. Ochiai, J. Fujita, T. Kaito, and S. Matsui, "Three-dimensional rotor fabrication by focused-ion-beam chemical-vapor-deposition," *Microelectronic engineering*, vol. 83, no. 4, pp. 1221–1224, 2006.

[70] A. Bohg, "Ethylene diamine-pyrocatechol-water mixture shows etching anomaly in boron-doped silicon," *Journal of the Electrochemical Society*, vol. 118, p. 401, 1971.

[71] P. Sievilä, N. Chekurov, and I. Tittonen, "The fabrication of silicon nanostructures by focused-ion-beam implantation and TMAH wet etching," *Nanotechnology*, vol. 21, p. 145301, 2010.

[72] J. Brugger, G. Beljakovic, M. Despont, N. F. de Rooij, and P. Vettiger, "Silicon micro/nanomechanical device fabrication based on focused ion beam surface modification and KOH etching," *Microelectronic engineering*, vol. 35, no. 1, pp. 401–404, 1997.

[73] N. Chekurov, K. Grigoras, A. Peltonen, S. Franssila, and I. Tittonen, "The fabrication of silicon nanostructures by local gallium implantation and cryogenic deep reactive ion etching," *Nanotechnology*, vol. 20, p. 065307, 2009.

[74] M. D. Henry, M. J. Shearn, B. Chhim, and A. Scherer, "Ga^+ beam lithography for nanoscale silicon reactive ion etching," *Nanotechnology*, vol. 21, p. 245303, 2010.

[75] J. Ziegler, M. D. Ziegler, and J. P. Biersack, "SRIM–The stopping and range of ions in matter (2010)," *Nuclear Instruments and Methods in Physics Research Section B: Beam Interactions with Materials and Atoms*, vol. 268, no. 11, pp. 1818–1823, 2010.

[76] T. Dai, X. Kang, B. Zhang, J. Xu, K. Bao, C. Xiong, and Z. Gan, "Study and formation of 2D microstructures of sapphire by focused ion beam milling," *Microelectronic Engineering*, vol. 85, no. 3, pp. 640–645, 2008.

[77] J. G. Mangum, D. T. Emerson, and E. W. Greisen, "The on the fly imaging technique," *Astronomy and Astrophysics*, vol. 474, no. 2, pp. 679–687, 2007.